Ocean Engineering 279 (2023) 114552

Contents lists available at ScienceDirect

Ocean Engineering

journal homepage: www.elsevier.com/locate/oceaneng

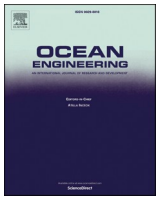

Marine propeller underwater radiated noise prediction with the FWH acoustic analogy Part 1: Assessment of model scale propeller hydroacoustic performance under uniform and inclined flow conditions

Savas Sezen [a,*], Mehmet Atlar [b]

[a] Lloyd's Register EMEA, Technical Investigation Department (TID), Southampton, UK
[b] Department of Naval Architecture Ocean, & Marine Engineering, University of Strathclyde, Glasgow, UK

ARTICLE INFO

Handling Editor: Prof. A.I. Incecik

Keywords:
AMR
Cavitation
CFD
DES
FWH
URN
The Princess Royal
TVC

ABSTRACT

This paper explores hydrodynamic performance, including cavitation and URN for the benchmark model scale propeller, The Princess Royal, operating under uniform and inclined flow conditions. In the numerical calculations, the DES method and the k-ω SST turbulence model were utilised to solve the cavitating flow around the propeller and determine the source field for the sound propagation. Also, the developed V-AMR advanced meshing technique was applied for accurately solving the tip vortex flow and hence better representation of the tip vortex cavitation in the propeller slipstream. The Schnerr-Sauer mass transfer model was used to model the cavitation on and off the propeller blades, whereas the cavitating propeller URN was predicted using the permeable formulation of the FWH equation. The numerical results were first validated with the available experimental data in model scale in a wide range of operating conditions through the propeller hydrodynamic performance characteristics, cavitation extensions and URN. Then, the numerical URN predictions were extrapolated to full-scale with the aid of the ITTC procedure to compare the CFD predictions with the extrapolated measured data obtained by different testing facilities within the scope of a recently conducted international round-robin test campaign. The results showed that the sheet and tip vortex cavitation was generally modelled successfully in the numerical calculations compared to the model-scale experimental observations in different facilities. The propeller URN predictions were in good agreement with the measured data in model scale, although some URN level discrepancies (i.e., around 5 and 10 dB) were observed between numerical predictions and model-scale measurements at certain frequencies in the low-frequency region of the noise spectrum. By taking the URN level differences measured in each facility into account, the full-scale extrapolated propeller URN predictions satisfactorily agree with the extrapolated full-scale experimental test data. Therefore, this study confirms that the CFD methods, together with the acoustic analogy, can be used for predicting the propeller URN, similar to other traditional ship hydrodynamic phenomena (e.g., resistance, self-propulsion, cavitation etc.).

1. Introduction

Considerable maritime transport and commercial shipping growth in the oceans has increased anthropogenic ambient underwater noise (URN) levels which have been surging over the last 50 years at both low (i.e., below 1 kHz) and mid (i.e., 1–20 kHz) frequency ranges (Hildebrand, 2004). The significant increase in URN levels induced by the shipping activities has negatively influenced the marine ecosystem since several marine mammals utilise sound actively as a primary source for their fundamental living activities such as communication, interaction, orientation, and feeding. Therefore, the rapid increase in ambient noise levels causes alteration in the behaviour of marine mammals and even endangers their survival (Hildebrand, 2005; Heise and Alidina, 2012).

Ship induced URN mainly consists of machinery noise, hydrodynamic flow noise induced by the hull flow, appendages and turbulence in the boundary layer, propeller noise, and machinery noise. Thus, understanding and interpreting different noise sources are crucial for monitoring ship-generated noise. Amongst different noise sources, propeller noise, which can be classified as non-cavitating and cavitating, is deemed to be the important noise source contributing to the overall URN

* Corresponding author.
E-mail address: savas.sezen@lr.org (S. Sezen).

https://doi.org/10.1016/j.oceaneng.2023.114552
Received 28 May 2022; Received in revised form 6 April 2023; Accepted 10 April 2023

levels, particularly when the propeller operates above the cavitation inception threshold (Abrahamsen, 2012). Under the condition that the propeller is heavily cavitating, the discrete peaks at blade passage frequencies and broadband part of the noise spectrum are considerably affected by the cavitation dynamics and hence cavitating propeller shadows the other noise sources (Aktas et al., 2016).

With an increase in environmental concerns regarding the potentially short and long-term detrimental effects of cavitating propeller URN on the marine ecosystem, several notations and non-mandatory guidelines have been published over the years to address the importance of URN. For instance, DNV GL (Det Norske Veritas Germanisher Lloyd) issued SILENT class notations in 2010 to highlight the noise-related issues and urge ship owners to take precautions to reduce URN emissions (DNV, 2010). Following this, International Maritime Organisation (IMO) published a non-mandatory guideline in 2014 and intended to advise the ship owners and designers, such as design specifications and maintenance of the hull and propeller, to reduce the URN radiated by commercial ships (IMO, 2014). Additionally, universities, conventions, regulatory bodies, experts, and national and international agencies have participated in different research projects supported by the EU (European Union) to understand and develop techniques to mitigate the URN (Chou et al., 2021). Between 2012 and 2015, two high-profile EC FP7 projects, AQUO (Achieve QUiter Oceans (AQUO, 2012),) and its counterpart, SONIC (Suppression of Underwater Noise Induced by Cavitation (SONIC, 2012),) were conducted to investigate the ship URN, prediction methods and impact on the marine environment including URN maps of European shipping. In recent years, SATURN (Solutions @ Underwater Radiated Noise (SATURN, 2021),) project, which is aimed to finish in 2025, has been underway to explore ship URN's detrimental effects on marine animals and develop effective mitigation techniques.

Over the past years, the international community has come together and discussed the information from different experts through international conferences, workshops, projects and studies to understand the importance of this issue. In the light of findings and discussions in this field, it has just been decided to review the IMO Guideline published in 2014 for reducing underwater noise from commercial shipping to address adverse impacts on marine life. These significant efforts devoted to the URN field point out that, in the near future, the new regulations related to URN will most likely come into force to mitigate its detrimental effects on the marine ecosystem, particularly in sensitive areas. Inevitably, this will increase the necessity of reliable and cost-effective computational and experimental procedures for assessing ship URN (Tani et al., 2019).

The Joint Research Programme (JRP), named Noise Measurements, was performed within the Hydro Testing Alliance Network of Excellence (HTA-NoE) to assess the propeller URN and investigate the experimental methods. This programme was successfully completed in 2011 (AMT'11, 2011). Later on, the members of JRP came together and decided to create a new research group called Noise Community of Practice (Noise CoP) of the Hydro Testing Forum (HTF), which was initially named Noise Working Group (NWG). The Noise CoP has performed a round-robin test (RR) campaign to explore cavitation and hydroacoustic performance of the newly introduced Newcastle University (UNEW)'s Deep-V type catamaran research vessel propeller, The Princess Royal (Atlar et al., 2013). In this RR test campaign, the aim is to explore the underwater radiated noise measurement techniques and compare the results obtained by different test facilities using the same benchmark propeller (i.e., The Princess Royal) (Aktas et al., 2016; Tani et al., 2020). The first systematic experiments of the RR test campaign were conducted in the Emerson Cavitation Tunnel of Newcastle University with the model scale Princess Royal propeller (Aktas et al., 2016). As a continuation of this study, the experimental set-ups, noise measurements techniques, cavitation observations and URN results were compared for the same propeller under the same operating conditions by different institutions (e.g., UNEW, UNIGE, MARIN, KRISO, NMRI, SSPA, CNR-INSEAN) (Tani et al., 2019, 2020). The results were obtained in model scale and then extrapolated to full-scale by the ITTC extrapolation procedure. The results obtained by different facilities showed some discrepancies in terms of propeller URN, whereas a good agreement was obtained for the cavitation extent with small differences. Thus, it was stated that further studies should be carried out to explore the possible reasons affecting the results (Tani et al., 2020).

While the experiments conducted in cavitation tunnels and depressurised towing tanks, empirical/semi-empirical methods are common approaches to predict the cavitation and propeller URN, the efforts for the prediction of propeller URN using the CFD (Computational Fluid Dynamics) tools have escalated considerably with the development of computational power and use of the hybrid methods, which are the combination of hydrodynamic solvers (e.g., potential and viscous based) and acoustic analogy. Although potential flow methods have been generally used together with the acoustic analogy for the propeller URN predictions because of their low computational cost, particularly in the preliminary design stage, they are not as capable as viscous based methods. The reason is that the turbulence and viscosity effects are disregarded, and hence this makes the potential methods inadequate for capturing the complex flow details, which are important for the accurate prediction of propeller URN. Therefore, viscous based CFD methods (e.g., RANS (Reynolds-averaged Navier Stokes), DES (Detached Eddy Simulation) and LES (Large Eddy Simulation)) together with the acoustic analogy are considered to be the state-of-art hybrid methods for the accurate prediction of propeller URN under non-cavitating and cavitating conditions. Amongst the different viscous CFD methods, DES and LES solve the vortex and turbulent structures in more detail than the RANS method. However, the LES method requires very fine grid structures and sufficiently small time-step resolution compared to DES, making it a computationally expensive CFD method, particularly for full-scale marine propeller applications. Therefore, DES, which combines RANS and LES methods, can be the most suitable method in terms of computational cost and resolving the flow details, including cavitating flow structures, both for model and full-scale CFD calculations (ITTC, 2017a; Sezen et al., 2021a).

With regards to acoustic analogy, the most commonly used acoustic analogy is the Ffowcs Williams Hawking (FWH) equation for both aeroacoustics and hydroacoustic problems. In the past, several studies were performed to understand the main noise mechanism and effectiveness of the methods used for the prediction of propeller hydroacoustic performance in open water and under uniform flow conditions (e.g., Ianniello et al., 2013; Lloyd et al., 2014; Ianniello and De Bernardis, 2015; Testa et al., 2018; Sezen et al., 2020; Sezen et al., 2021b; Stark and Shi, 2021). Similarly, the cavitating propeller URN predictions are of great interest using the hybrid methods as cavitation is the most important noise source, and its avoidance is generally not possible in a wide range of operating conditions, especially for commercial vessels. Although several cavitation types occur on and off the blades, the most common observed cavitation pattern on ship propellers is the combination of sheet and tip vortex cavitation (TVC) (Bosschers, 2018). The cavitating propeller URN in the presence of only sheet cavitation was predicted in the low-frequency region of the noise spectrum using the potential based panel method and time domain acoustic analogy based on the FWH equation by Seol et al. (2005). The predicted results were found to agree with those of other numerical results. It was stated that more study was needed to include the non-linearities and complexities created by sheet cavitation break-off and formation of the tip vortex cavitation to predict the high-frequency range of noise spectrum. Lidtke et al. (2015) presented preliminary results for the Potsdam Propeller Test Case (PPTC) in cavitating and open water conditions using RANS and porous formulation of FW-H acoustic analogy. The study aimed to explore the influence of different integration surfaces on overall noise levels and understand the individual noise terms. The results showed that the unsteady behaviour of the cavities and associated broadband noise spectrum could not be predicted accurately because of the inherent modelling

deficiencies of the RANS method. Kimmerl et al. (2021) explored the propeller URN, pressure pulses on the hull both under uniform and non-uniform flow conditions using ILES (Implicit Large Eddy Simulation) and porous formulation of FW-H equation. In order to model the tip vortex cavitation (TVC) in the propeller slipstream, the *Q* criterion-based priori mesh refinement was employed. The hydroacoustic results and hull-pressure fluctuations showed good agreement with certain discrepancies up to 20 dB at certain frequencies compared to experimental data. In a previous study by the authors (i.e., Sezen et al., 2021a), we explored the flow around the model scale propeller, including cavitation and propeller hydroacoustic performance using RANS and DES methods. The detailed flow investigation was carried out using RANS and DES methods and found out that the RANS method failed to capture the flow details inside the vortex core compared to the DES method. This resulted in insufficient modelling of TVC in the propeller slipstream. The hydroacoustic results were also compared with the experimental data at one operating condition in model scale and good agreement was found between CFD and experiment with some discrepancies.

Despite the several studies under non-cavitating and cavitating conditions using potential and viscous based methods with the FW-H based acoustic analogy for the propeller URN predictions, the verification and validation studies with the available experimental data are rather scarce due to the lack of experimental data for the benchmark propellers in the literature. This makes the capabilities of the hybrid CFD methods questionable for the propeller URN predictions. For this reason, the reliability of the CFD tools for the propeller URN predictions has not been completely understood compared to model scale experiments performed in either cavitation tunnels or depressurised towing tanks. Therefore, the present study aims to fill this research gap by conducting a comprehensive validation study using the state-of-art hybrid method with the available experimental data obtained by different facilities in the scope of the RR test campaign for the newly introduced benchmark propeller (i.e., The Princess Royal). In this way, the reliability and capabilities of the hybrid CFD method were shown at different operating conditions both in model and full-scale in comparison with the experimental data in the presence of sheet and tip vortex cavitation.

In this study, the cavitating flow around the benchmark propeller was solved using a high-fidelity DES method together with the k-ω SST turbulence model in the facilities of Star CCM+ (Star CCM+ 14.06, 2019). The sheet and tip vortex cavitation were modelled using the Schnerr Sauer mass transfer model. The Vorticity-based Adaptive Mesh Refinement procedure (V-AMR), which was developed and proposed by the authors (Sezen and Atlar, 2021), was utilised for better realisation of the TVC in the propeller slipstream. The numerical calculations were conducted under uniform and inclined conditions. First, the hydrodynamic performance characteristics and cavitation observations were compared with the available experimental data obtained by different facilities in the scope of the RR test campaign. Following this, the hydrodynamic solver was coupled with the FW-H acoustic analogy to predict the propeller URN at different receiver configurations similar to experiments. The convergence of the FW-H solution was shown using the different porous/permeable surfaces. The verification of the URN calculations was also shown with the comparison of hydrodynamic and hydroacoustic pressures in the near field. URN results were first compared with the experimental data measured in the GENOA cavitation tunnel in a model scale under uniform flow conditions. Later on, the numerical results were extrapolated to full-scale to compare them with those of other results obtained by different facilities during the RR test campaign under uniform flow conditions. The presented hybrid approach's capabilities and accuracy were discussed in terms of cavitation.

The hydroacoustic performance of The Princess Royal propeller was predicted under uniform flow conditions in our Part 1 study. In the continuation part of this study (i.e., Part 2), the numerical investigations were performed for the same benchmark propeller operated under non-uniform flow conditions, corresponding to the full-scale operating conditions. Following this, the numerical calculations were also carried out in full-scale in the presence of a hull, and the reliability of the presented approach was shown at the far-field where the sea-trial data was collected in our Part 3 study.

The structure of the paper is organised as follows. The methodology is presented in Section 2. The test case and numerical modelling details (e.g., computational domain, grid structure, etc.) are given in Section 3. The numerical results, including cavitation observations and URN predictions, are presented and discussed in Section 4. Consequently, the concluding remarks are given in Section 5.

2. Theoretical background

2.1. Hydrodynamic model

The governing flow equations were solved using the commercial CFD solver, Star CCM+ 14.06 (Star CCM+ 14.06, 2019). In the numerical calculations, the Delayed Detached Eddy Simulation (DDES) variant of the DES method and the k-ω SST turbulence model were utilised due to the several drawbacks of RANS and the higher computational cost of the LES methods. DES method uses the features of both the RANS method for the attached boundary layer and irrotational flow regions and the LES method for the unsteady separated regions. The switch from RANS to LES is driven by the local grid spacing relative to the distance to the wall, and thus suitable grid design is crucial for the accuracy of the DES solution. The DES formulation of the k-ω SST turbulence model is derived by changing the dissipation term in the transport equation for the turbulent energy. In this method, the specific dissipation rate ω in the transport equations is replaced by $\widetilde{\omega}$,

$$\widetilde{\omega} = \omega\varphi \tag{1}$$

and φ can be defined as;

$$\varphi = \max(l_{ratio}F, 1) \tag{2}$$

where, l_{ratio} (i.e., length scale ratio) is calculated as;

$$l_{ratio} = \frac{l_{RANS}}{l_{LES}} \tag{3}$$

Here, l_{RANS} and l_{LES} can be written as;

$$l_{RANS} = \frac{\sqrt{k}}{f_{\beta^*}\beta^*\omega} \tag{4}$$

$$l_{LES} = C_{DES}\Delta \tag{5}$$

Here, k is the turbulent kinetic energy, f_β is the free-shear modification factor, β^* is a model coefficient of turbulence model, Δ is the biggest distance between the cell centre of neighbour cell centre and cell centre under consideration, and C_{DES} is the model coefficient, which blends the values obtained from the independent calibration of the k-epsilon and k-ω versions of the k-ω SST model. In Equation (2), the F can be defined as;

$$F = 1 - F_2 \tag{6}$$

where F_2 is the blending function defined in the turbulent eddy viscosity formulation for the k-ω SST turbulence model. In Equation (2), when the $\varphi = 1$, the solution is provided by the RANS method, whereas $\varphi > 1$ shows the regions where the LES method is used in the DES method (Spalart et al., 1997 and Star CCM+ 14.06, 2019). In our case, the suitability of the adopted cells for the boundary layer and propeller slipstream (i.e., to understand where the RANS and LES methods are used) can be visualised using the DES correction factor (i.e., F_{DES}). As shown in Fig. 1, the boundary layer solution is provided by RANS, whereas LES is used for the flow field solution in the propeller slipstream, as expected. Also, the far-field where the coarse grid is present is

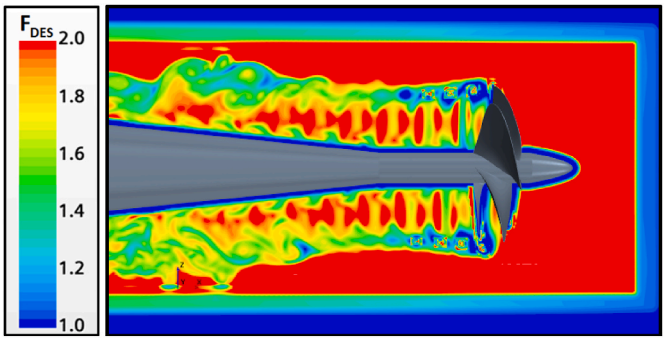

Fig. 1. Contour plots of DES Correction Factor (RANS is $F_{DES} = 1$ and LES is $F_{DES} > 1$).

solved using the RANS method.

Cavitation occurs when the pressure at a specific location within a liquid is below the saturation vapour pressure of the liquid. The cavitation modelling in the numerical solver is based on the homogeneous two-phase flow assumption. First, the equations of the motion are solved for a single effective fluid. The additional equation is used to determine the vapour and liquid phase distribution for the vapour volume fraction. In this approach, all nuclei initially have the same radius, and nuclei are spherical and uniformly distributed within the liquid. The numerical calculations used the Schnerr-Sauer cavitation model, based on a reduced Rayleigh-Plesset equation. In this cavitation model, the influence of bubble growth acceleration, viscous effects and surface tension effects are neglected (Schnerr and Sauer, 2001; Star CCM+ 14.06, 2019).

2.2. Hydroacoustic model

The hybrid method, which is the combination of the hydrodynamic method and acoustic analogy, was used to predict the propeller URN. The source and acoustic propagation fields are decoupled using the hybrid method. The source field is first determined with the hydrodynamic solver (i.e., in our case with the DES method), and acoustic propagation is provided using the acoustic analogy. An acoustic analogy is used as a post-processing tool to predict the sound using the numerical solutions of the flow field provided by the hydrodynamic solver. Amongst the different acoustic analogies (e.g., Lighthill, 1952; Curle, 1955), Ffowcs Williams Hawkings (Ffowcs Williams and Hawkings, 1969) analogy, which is the extended version of Lighthill's analogy (Lighthill, 1952), is the most commonly used analogy in aeroacoustics and hydroacoustic fields. Lighthill's equation does not take into consideration the presence of solid surfaces, whereas the Ffowcs Williams Hawkings (Ffowcs Williams and Hawkings, 1969) incorporates the influence of surfaces in arbitrary motion for moving and permeable surfaces. The integral form of the FWH equation consists of surface and volume integrals for the sound representation. The monopole (i.e., thickness) and dipole (i.e., loading) noise terms are evaluated using the surface integrals, while the quadrupole noise sources (i.e., nonlinear) are computed using the volume integrals. In aeroacoustics problems, the quadrupole noise sources are generally ignored when the Mach number is low, but its contributions are included in transonic and supersonic regimes. However, unlike the aeroacoustics fields, the nonlinear noise sources, mainly represented by turbulence and vorticity, significantly contribute to the overall acoustic pressure levels under non-cavitating conditions (Ianniello et al., 2013). Similarly, they can also contribute to the overall noise levels even if the cavitation related linear noise sources (i.e., monopole or thickness) are dominant in the presence of cavitation. Due to this reason, the contribution of nonlinear noise sources, including TVC, can be included effectively using the permeable formulation of the FWH equation, which was first applied and proposed by Ffowcs Williams and Hawkings (1969) and suggested as a possible solution for the FWH equation by Di Francescantonio (1997). In the permeable FWH equation, the new modified velocity (U) and modified stress tensor (L) variables are introduced. The main advantage of using permeable surfaces is that the direct solution of the volume integrals is more computationally expensive (Ianniello et al., 2013). Thus permeable FWH reduces the cost of the numerical solution. Also, the solution of the volume integrals in the generalised FWH equation is more sensitive to the numerical errors and accuracy of the hydrodynamic data compared to the solution of surface integrals in the permeable formulation.

The permeable formulation of the FWH equation can be written by taking the newly introduced variables (i.e., U_i and L_i) into account using the generalised FWH equation (Farassat, 2007);

$$\Box^2 p = \frac{\partial}{\partial t}\left[\rho_0 U_n \delta(f)\right] - \frac{\partial}{\partial x_i}\left[L_i n_j \delta(f)\right] + \frac{\partial^2 T_{ij}}{\partial x_i \partial x_j} \tag{7}$$

Here, $\Box$ is the wave or D'Alembert operator in three-dimensional space, n is unit outward normal, ρ_0 is the speed of density in the undisturbed medium, p is the acoustic pressure, T_{ij} is the Lighthill stress tensor. $\delta(f)$ is the Dirac delta function. The derivation of the FWH equations and comprehensive mathematical formulations can be found in the studies of Farassat (2007) and Brentner and Farassat (2003).

In this equation, the first two terms are the pseudo-thickness and pseudo-loading noise contributions respectively. The third term represents the quadrupole noise sources outside of the integral surface. The undamped fluctuating pressure and momentum as nonlinear noise sources pass through the boundaries of permeable surfaces can produce spurious noise that can contaminate the overall acoustic pressures. This spurious noise occurs because of the truncation errors of the source terms at the permeable surface boundary. This problem is also known as the "end cap" or closure problem (Nitzkorski, 2015). The receivers located upstream are less sensitive to the effects of spurious noise as the linear thickness and loading terms are dominant. However, the receivers located downstream of the propeller can be strongly affected by spurious noise. The end-cap problem is associated with the differences between acoustic and hydrodynamic pressure distributions described in Ffowcs Williams, 1992 (Testa et al., 2021). Several approaches are used to correct the end cap problem in the near field using the corrected volume terms (e.g., Wang et al., 1996; Ikeda et al., 2017).

Nevertheless, the applications of these alternative approaches may not be practical for different problems (Lidtke et al., 2019a). In order to reduce the spurious noise, the permeable surface can be placed far from the flow region where the vorticity is still present. However, this leads to the risk of information loss because of the numerical dissipation and discretisation errors. Even if one can attempt to adopt fine grid resolution for the entire large permeable surface to minimise the numerical dissipation, inevitably, this will increase the computational cost of the solution and it is not practical. Alternatively, this issue can be eliminated completely by solving the full FWH equation, including the nonlinear noise sources outside of the permeable surface. However, calculating volume terms to account for the contribution of nonlinear noise sources outside of the permeable surface is computationally expensive and difficult to compute and retain data. Thus, in our study, in order to reduce the computational cost of the solution, the contribution of possible nonlinear noise sources outside of the permeable surface was neglected. Also, the investigation of the end-cap problem was left out of the scope of this study. The several permeable surfaces, which were placed inside the fine grid region with different dimensions, were tested to show the convergence of the solution.

3. Test case set-up and numerical modelling

3.1. Propeller geometry and test matrix

The new benchmark Newcastle University's (UNEW) Deep-V type

catamaran research vessels' propeller (i.e., The Princess Royal) was selected in this study as the round-robin (RR) test campaign has been conducted by different facilities (i.e., MARIN, UNIGE, SSPA, UNEW, KRISO, NMRI and CNR-INM) for this model propeller. The main particulars and 3D view of the five-bladed model propeller are given in Table 1 and Fig. 2, respectively.

Tests have been carried out for the cavitation observations and noise predictions for the selected propeller in the scope of the ongoing RR test campaign. The model scale propeller's diameters used in different facilities are slightly different, and they are taken as 0.25m, 0.22m, and 0.214m. So far, the tests were conducted under uniform and inclined flow conditions by taking either the thrust coefficient identity (i.e., K_T) or advance ratio (i.e., J) identity (Tani et al., 2019, 2020). The operational conditions set according to the RR test campaign are described in Table 2. As shown in Table 2, uniform (i.e., level) and inclined shaft flow configurations together with six operating conditions are explored in this study through hydrodynamic performance prediction, cavitation observation and noise prediction. The operating conditions were changed according to advance ratio (i.e., J) and cavitation number based on propeller rotational speed (n) as follows;

$$J = \frac{V_A}{nD} \tag{8}$$

$$\sigma_N = \frac{P_0 - P_V}{0.5\rho(nD)^2} \tag{9}$$

3.2. Numerical modelling

3.2.1. Computational domain and boundary conditions

In the numerical calculations, the computational domain dimensions were set according to the dimensions of the GENOA cavitation tunnel measurement section, which has a 2.2m total length and 0.57m × 0.57m square test section. Similarly, the upstream and downstream of the computational domain from the propeller blades' centre were extended around 2.5D and 7.5D, respectively. The width and height of the domain were also set to 0.57m × 0.57m, respectively. As shown in Fig. 3, the positive X direction was identified as velocity inlet, whereas the negative X direction was defined as pressure outlet. The remaining surfaces of the domain, propeller, shaft, and hub were defined as no-slip walls. The computational domain consisted of three different regions static, rotating and noise. These regions connected each other with the internal interfaces. The rotating region was used for the propeller motion, whereas the noise region created using permeable surface was utilised for the propeller URN predictions. For the inclined shaft conditions, the same computational domain was used with shaft inclination.

3.2.2. Grid generation

The grid quality used in numerical calculations is of paramount importance for representing the complex geometry and the accurate solution of the flow field. In order to reduce the discretisation errors, the grid resolution should be sufficient enough to resolve all the relevant flow features, including cavitation dynamics, around the propeller. The numerical modelling of cavitation phenomena is complicated compared to non-cavitating conditions because of the cavitation dynamics and turbulence interactions. Thus, a suitable grid resolution should be adopted in numerical calculations. In particular, an accurate solution of tip vortex flow is strongly dependent on grid resolution. For this reason, advanced mesh techniques should be implemented around the tip vortex regions to predict the minimum pressure inside the vortex accurately. In this regard, the authors have recently introduced the Vorticity-based Adaptive Mesh Refinement (V-AMR) technique for the solution of the tip vortex flow and hence tip vortex cavitation (TVC) observation in the propeller slipstream (Sezen and Atlar, 2021). Using the V-AMR technique, the grid is refined as local as possible in the vicinity of tip vortex areas to reduce the computational cost of the solution. This technique consists of two stages, namely 1st stage V-AMR and 2nd stage V-AMR. This two-stage V-AMR procedure enables to reduce the computational cost of the solution. In the 1st stage, the relatively coarse grid reveals the tip vortex trajectory in the propeller slipstream. Following this, 2nd stage V-AMR is implemented using the fine grid resolution. The authors have shown the feasibility and accuracy of this technique with different benchmark propellers using different numerical methods (e.g., RANS, DES and LES). Therefore, in this study, the same V-AMR technique was implemented to observe TVC under uniform and inclined shaft configurations given in Table 2. Detailed information about the application of this technique can be found in the study conducted by the authors (Sezen and Atlar, 2021).

The grid quality is also crucial for the accurate prediction of propeller URN as the sound is propagated from near field to far-field. Thus, the numerical diffusion should be as minimum as possible. Also, the insufficient grid resolution and abrupt mesh changes inside the noise surface can lead to non-physical numerical noise, which is mainly created by the sliding mesh interfaces, and they can contaminate the overall acoustic pressure. In a recent study by the authors (Sezen et al., 2021b), the influence of grid resolution on propeller hydroacoustic performance was comprehensively investigated, and it was shown that the hydroacoustic performance of propellers was more dependent on grid resolution compared to the prediction of global performance characteristics such as thrust, torque and efficiency. Thus, in this study, based on our recent investigation, the uniform grid resolution in all directions was applied, and the permeable surface was located inside the fine grid region to minimise the information loss because of the numerical dissipation. The adopted grid structure can be seen in Fig. 4.

In this study, the trimmer mesh with hexahedral elements was adopted using the Star CCM + automated mesh tool to solve the flow around the cavitating propeller and URN predictions at various operating conditions given in Table 2 (Star CCM+ 14.06, 2019). The grid was refined in all directions to achieve the $y^+ < 1$ to resolve the boundary layer itself in order to increase the accuracy of the solution. In order to observe the TVC, the V-AMR technique was also implemented using the mesh table based on user-based field functions. In order to reduce numerical noise, the high-quality cells with minimum skewness were utilised in all directions. The grids were also aligned at the transition regions to decrease the possible numerical noise sources arising from the internal interfaces. The total element count was calculated at approximately 23M for each case.

3.2.3. Analysis properties

The application of the DES method can be challenging unless suitable simulation properties are selected. In the numerical calculations, a segregated flow solver and a SIMPLE algorithm were used to compute the velocity and pressure. The Hybrid Bounded Central Differencing Scheme (Hybrid-BCD) was used for the segregated solver to discretise convection terms in the momentum equations. This scheme blends second-order upwind and bounded central differencing, and the blending factor is calculated according to the flow field features. This discretisation scheme is also advisable for DES methods. Furthermore, the second-order discretisation scheme was also utilised for the convection of turbulence terms (Star CCM+ 14.06, 2019).

The second-order implicit numerical scheme was used for the time discretisation. For the DES method, the time step selection is also an

Table 1
The main particulars of the propeller (Atlar et al., 2013).

Parameters	Model Scale Princess Royal Propeller
Diameter, D (m)	0.22
P/D at 0.7R	0.8475
Expanded Blade Area Ratio (EAR)	1.057
Blade Number, Z	5
Rake (°)	0
Skew (°)	19

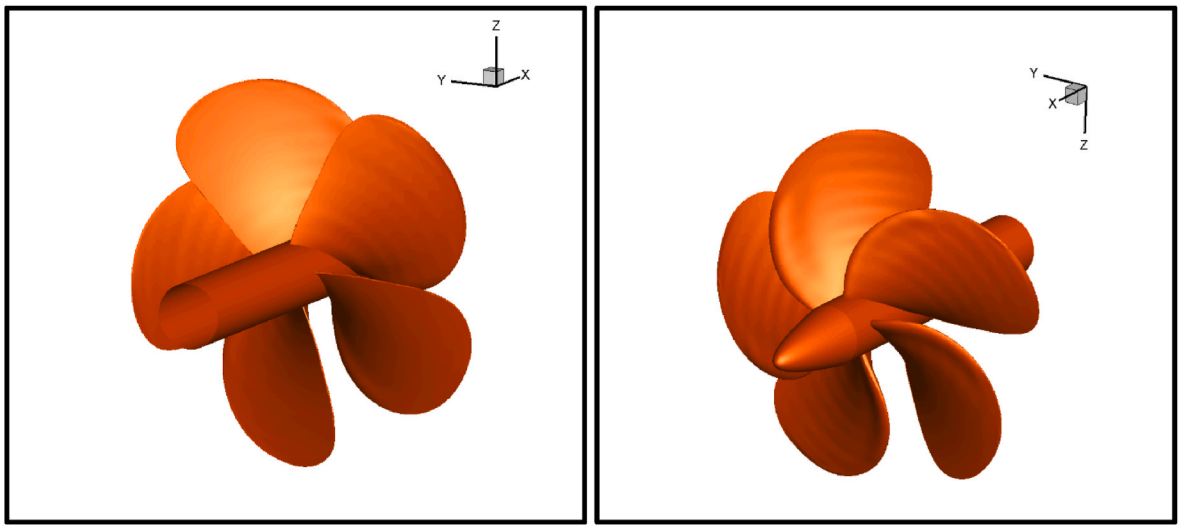

Fig. 2. 3D view of the benchmark Princess Royal propeller.

Table 2
Test matrix.

Test Condition	J	β (°)	σ_N	V_A	n (*rps*)
C1	0.4	0	2.223	3.08	35
C2	0.4	0	1.311	3.08	35
C3	0.4	0	0.721	3.08	35
C4	0.5	0	3.486	3.85	35
C5	0.5	0	2.024	3.85	35
C6	0.5	0	1.137	3.85	35
C7	0.4	5	2.223	3.08	35
C8	0.4	5	1.311	3.08	35
C9	0.4	5	0.721	3.08	35
C10	0.5	5	3.486	3.85	35
C11	0.5	5	2.024	3.85	35
C12	0.5	5	1.137	3.85	35

Here, V_A is the inflow speed, n is the propeller rotation rate, P_0 is the static pressure, P_V is the vapour pressure, and ρ is the water density.

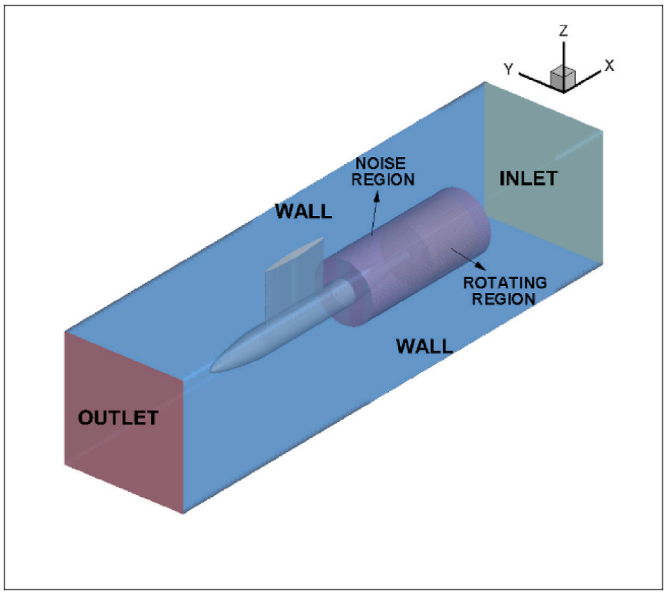

Fig. 3. Representation of computational domain used in the numerical calculations.

important parameter linked to the CFL number inside the domain. In this regard, the time-step was selected as 0.5° of the propeller rotational rate (i.e., 3.96×10^{-5}) at different operating conditions. This timestep was kept constant while collecting the acoustic pressures in the hydro-acoustic part of the solution. As the implicit scheme was utilised, the CFL number is not associated with the stability of the time scheme, but keeping the CFL around 1, especially in the propeller slipstream, enabled to increase the accuracy of the numerical solution. However, CFL number increased in the adaptive mesh refinement regions due to the decrease in mesh sizes.

The multiphase VOF (Volume of Fraction) approach was coupled with the cavitation model for modelling the cavitation phenomena. For the convection term of the VOF approach, High-Resolution Interface Capturing (HRIC) was used to track the sharp interfaces between phases. The Schnerr- Sauer mass transfer model based on the reduced Rayleigh-Plesset equation was used to model the cavitation. In this model, the customisable cavitation parameters (i.e., nuclei density and diameter) were taken as default values based on our recent investigation of its effects on the sheet and tip vortex cavitation formation (Sezen and Atlar, 2021). Thus, the nuclei density and diameter were set to 10^{12} ($1/m^3$) and 10^{-6} (m), respectively.

The DES method was initialised with a steady-state RANS method using the k-ω SST turbulence model. In this way, the DES method's robustness was increased and the RANS solution provided a consistent initial guess that ensured that the problem was mathematically well-posed. After initialising with the RANS method, the solver was switched to the DES method by activating the cavitation. When the flow field converged, the acoustic analogy was started to collect the acoustic pressures at the specified points using the receivers. The acoustic data were collected during the six propeller revolutions.

At the initialisation stage with the steady RANS method, the Moving Reference Frame (MRF) technique was used to model the propeller rotational motion. When the solver was switched to the DES method, the propeller rotational motion technique was changed with the Rigid Body Motion (RBM). During the first propeller rotation, the time-step was set to 1° of propeller rotational rate and then reduced to 0.5° of propeller rotational rate. In this way, any possible numerical stability issues related to cavitation phenomena were avoided.

4. Results

In this section, the hydrodynamic and hydroacoustic results, including cavitation observations, are first given for the model scale propeller. Following this, the numerical results are extrapolated to full-

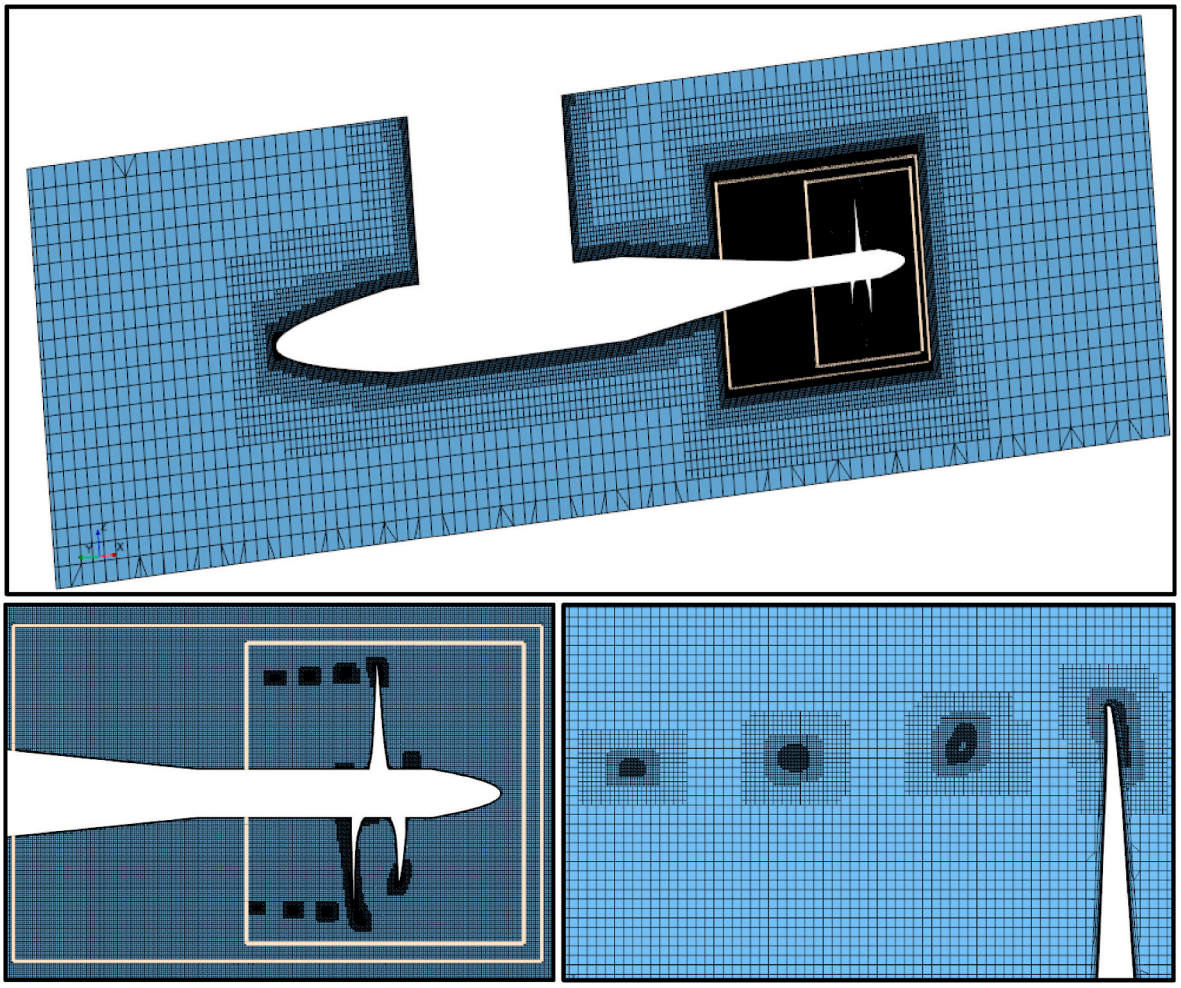

Fig. 4. Representation of grid resolution in the computational domain, permeable surface, and tip vortex areas.

Table 3
Adapted cavitation numbers for different operating conditions in the scope of the RR test campaign (Tani et al., 2020) and CFD.

	σ_N							
Condition	MARIN	UNIGE	SSPA	UNEW	KRISO	NMRI	CNR	CFD
C1	2.57	2.223	2.340	2.220	2.140	3.081	2.730	2.223
C2	1.296	1.311	1.410	1.300	1.300	1.442	1.590	1.311
C3	0.720	0.721	0.790	0.720	1.130	0.801	0.880	0.721
C4	3.475	3.486	3.630	3.480	3.320	2.978	3.890	3.486
C5	2.025	2.024	2.130	2.030	2.030	2.173	2.270	2.024
C6	1.125	1.137	1.180	1.130	1.120	1.207	1.260	1.137
C7	–	2.223	–	–	–	–	–	2.223
C8	–	1.311	–	–	–	–	–	1.311
C9	–	0.721	–	–	–	–	–	0.721
C10	–	3.486	–	–	–	–	–	3.486
C11	–	2.024	–	–	–	–	–	2.024
C12	–	1.137	–	–	–	–	–	1.137

scale using the ITTC scaling procedure as in the experiment and compared with those obtained results by different facilities in the scope of the RR campaign under uniform flow and level shaft conditions.

4.1. Model scale propeller

4.1.1. Hydrodynamic results

In the scope of the RR test campaign, the participants carried out the tests at thrust coefficient identity (i.e., $K_T = 0.242$ and $K_T = 0.192$, corresponding to $J = 0.4$ and $J = 0.5$, respectively) or J identity. This resulted in slightly different thrust and torque values and hence operating conditions (Tani et al., 2020). Also, in order to keep the advance ratio (J) constant, slightly different cavitation numbers (σ_n) were used when the thrust identity was adopted during the tests, as given in Table 3. In CFD calculations, the J identity was adopted as several iterations were required to equal the thrust coefficients between CFD and experiment. This would increase the computational cost of the solution for twelve operating conditions. As the model scale hydrodynamic and hydroacoustic results obtained by CFD were mainly compared with the data obtained by the University of Genoa Cavitation tunnel (UNIGE), the same cavitation numbers as in the UNIGE tunnel were adopted in CFD computations for a range of operating conditions.

Table 4 shows the thrust coefficients obtained by CFD and experiments performed by different facilities. As shown in Table 4, CFD results are in good agreement with those of experimental data obtained by SSPA and NMRI, as they mainly used the J identity throughout the tests. Also, the comparison of CFD results with those of experimental data obtained by other facilities (i.e., MARIN, UNIGE, UNEW, KRISO and CNR) shows that the deviation is between 5% and 7% in terms of thrust coefficient, depending on the operating conditions. It should be noted that similar to other facilities, except CNR, the propeller was operating in pulling configuration in the CFD computations.

4.1.2. Cavitation extensions

The cavitation observations obtained by CFD are first compared in Fig. 5 to show the change in cavitation extensions at different operating conditions (i.e., the level and inclined shaft configurations) before comparing them with the experimental data obtained by different facilities. The general comments for the cavitation observations at all operating conditions can be summarised as follows.

- ➢ The suction side sheet cavitation is present at all operating conditions, except C4.
- ➢ With an increase in blade loading from C1 to C3 at $J = 0.4$ and C4 to C6 at $J = 0.5$, the sheet cavitation extension and its thickness increase.
- ➢ Similar sheet cavitation phenomena and dynamics are observed at C1, C2, C5 and C6, with differences in their extensions.
- ➢ Leading-edge vortex cavitation is observed at C1, C2, C3 and C6.
- ➢ Stable TVC occurs at C1, C2 and C6 with different extensions in the propeller slipstream. The strongest TVC in the propeller slipstream is observed at C2.
- ➢ The largest sheet cavitation is observed at C3 with rather unstable vortex cavitation. This unsteadiness affects the vortex structure considerably, resulting in tip vortex core disruption.
- ➢ The cavitation extensions in inclined shaft configurations are slightly different from level shaft configurations.

Following the comparison of cavitation extensions obtained by CFD at different operating conditions, the numerical results are also compared with the experimental observations obtained by different facilities within the scope of the RR test campaign. Fig. 6 shows the comparison of cavitation extensions for C1, C2 and C3 at $J = 0.4$. As shown in Fig. 6, similar sheet and tip vortex cavitation are observed during the experiments with slight differences. The sheet cavitation is slightly more extended towards the inner radii in CFD compared to experimental observations at C1, C2 and C3. The application of the V-AMR technique in numerical calculations enables better modelling of the TVC in the propeller slipstream. Nevertheless, the TVC observed in the CFD is less extended in the propeller slipstream than in the experiments. Amongst the conditions, the more extended TVC in the propeller slipstream is captured at C2 as the vortex diameter is sufficiently bigger than those of C1 and C3. The unstructured and cloudy appearance of TVC at C3 could not be observed in CFD as observed in the experiments.

Fig. 7 shows the comparison of cavitation observations between CFD and experiment for C4, C5 and C6 at $J = 0.5$. Similar sheet cavitation dynamics and extensions are observed in CFD compared to experiments for C5 and C6. In the experiments, the weak TVC, which is attached to the blade leading edge (i.e., NMRI) or appears incipient in the propeller slipstream, is observed for C4 by other facilities. Unlike the experiments, the weak TVC formation could not be observed in CFD for C4 and C5. The reason is that the diameter of the tip vortex is rather small at these operating conditions. Due to this fact, the adopted grid size inside the vortex core (i.e., 0.2 mm) using the V-AMR technique may not be sufficient to capture the weak cavitation dynamics in the CFD.

Similar to level shaft configuration, the cavitation observations are compared between CFD and experiment for the inclined shaft configurations in Fig. 8. As the RR test campaign data is not yet published for inclined shaft configuration, the numerical results are only compared with the experiments performed in UNIGE. Akin to the level shaft configuration, analogous sheet cavitation dynamics are observed amongst the conditions. The sheet cavitation is generally more extended towards inner radii in CFD compared to experiments. Also, the same TVC dynamics in the propeller slipstream could not be captured for C10 and C11 due to the small diameter of TVC in the propeller slipstream observed in the experiment.

Investigating the details of the cavitation phenomena, such as thickness and chordwise extensions between CFD and experiment, is rather difficult as the cavitation patterns were observed at different

Table 4
The comparison of thrust coefficients between experiments (Tani et al., 2020) and CFD at different operating conditions.

	K_T							
Condition	MARIN	UNIGE	SSPA	UNEW	KRISO	NMRI	CNR	CFD
C1	0.223	0.244	0.260	0.242	0.255	0.243	0.245	0.262
C2	0.243	0.244	0.262	0.242	0.255	0.243	0.245	0.262
C3	0.222	0.226	0.236	0.242	0.255	0.243	0.232	0.237
C4	0.192	0.190	0.203	0.190	0.203	0.191	0.189	0.202
C5	0.193	0.189	0.204	0.190	0.203	0.191	0.191	0.203
C6	0.195	0.191	0.206	0.190	0.203	0.191	0.195	0.207
C7	–	0.245	–	–	–	–	–	0.261
C8	–	0.245	–	–	–	–	–	0.262
C9	–	0.226	–	–	–	–	–	0.237
C10	–	0.189	–	–	–	–	–	0.202
C11	–	0.190	–	–	–	–	–	0.204
C12	–	0.192	–	–	–	–	–	0.207

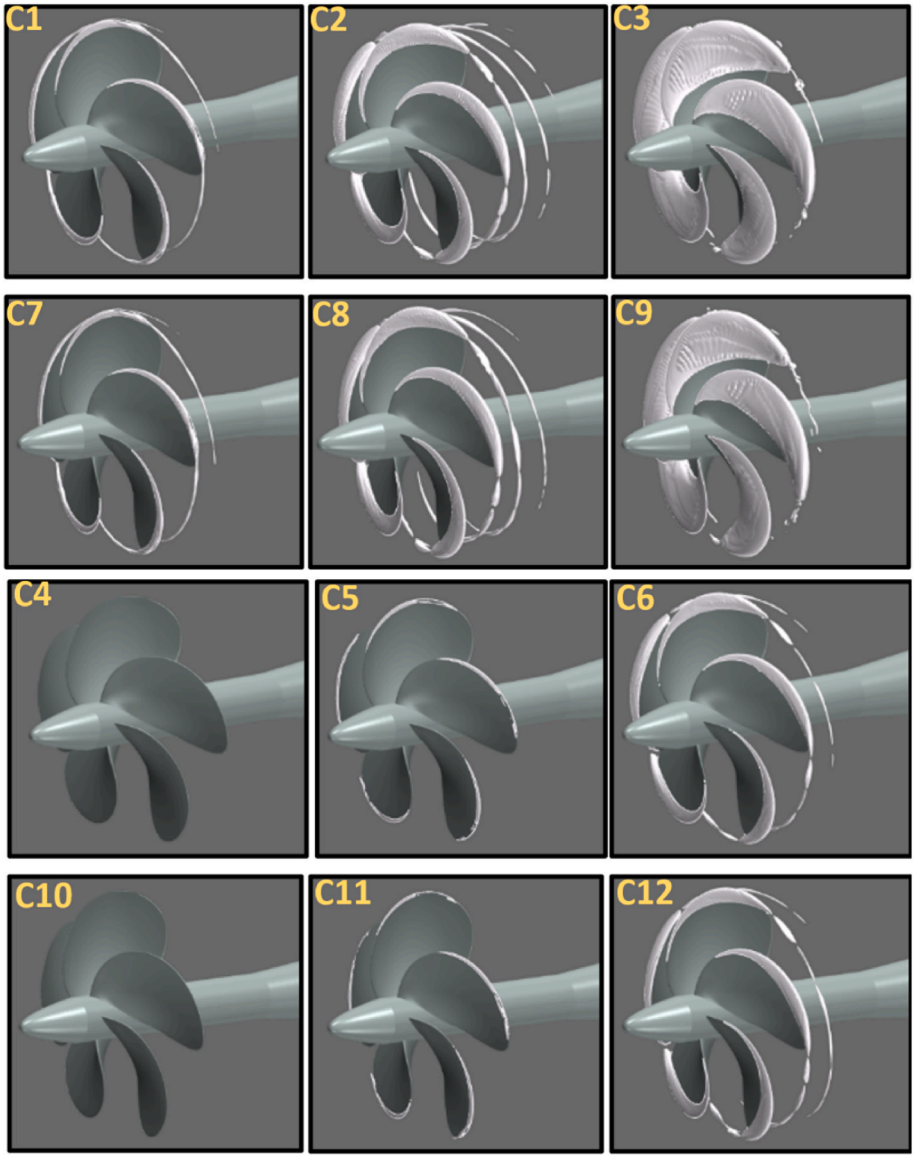

Fig. 5. Comparison of cavitation extensions between uniform and inclined flow conditions at several operating conditions ($\alpha_v = 0.1$).

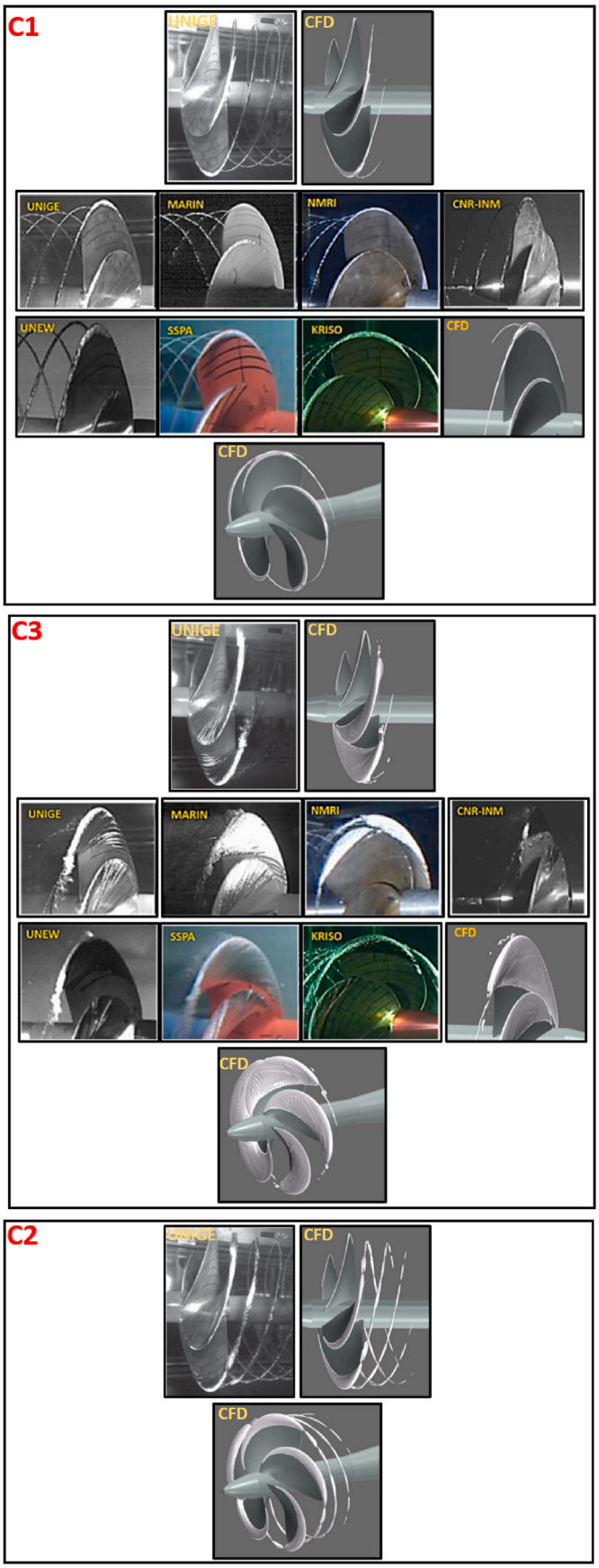

Fig. 6. Comparison of cavitation extensions at $J = 0.4$ for level shaft configurations (C1, C2 and C3) ($\alpha_v = 0.1$).

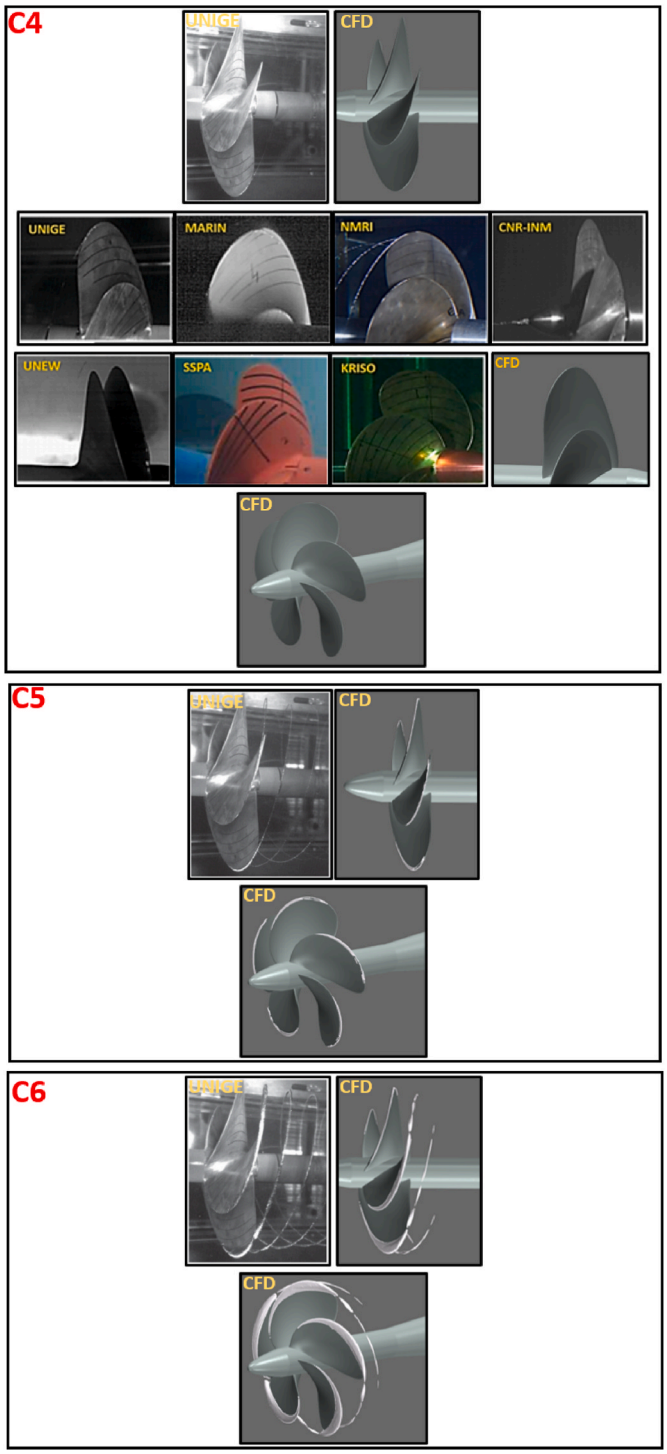

Fig. 7. Comparison of cavitation extensions at $J = 0.5$ for level shaft configurations (C4, C5 and C6) ($\alpha_v = 0.1$).

angles by different facilities during the experiments, as stated in Tani et al. (2020). Nevertheless, similar sheet cavitation together with less TVC extensions is observed in CFD compared to experiments. The differences between the experiments and CFD can be associated with several effects such as the development of boundary layer, Reynolds number, water quality and freestream turbulence. A detailed comparison of the cavitation observations obtained by each facility can be found in the study of Tani et al. (2020).

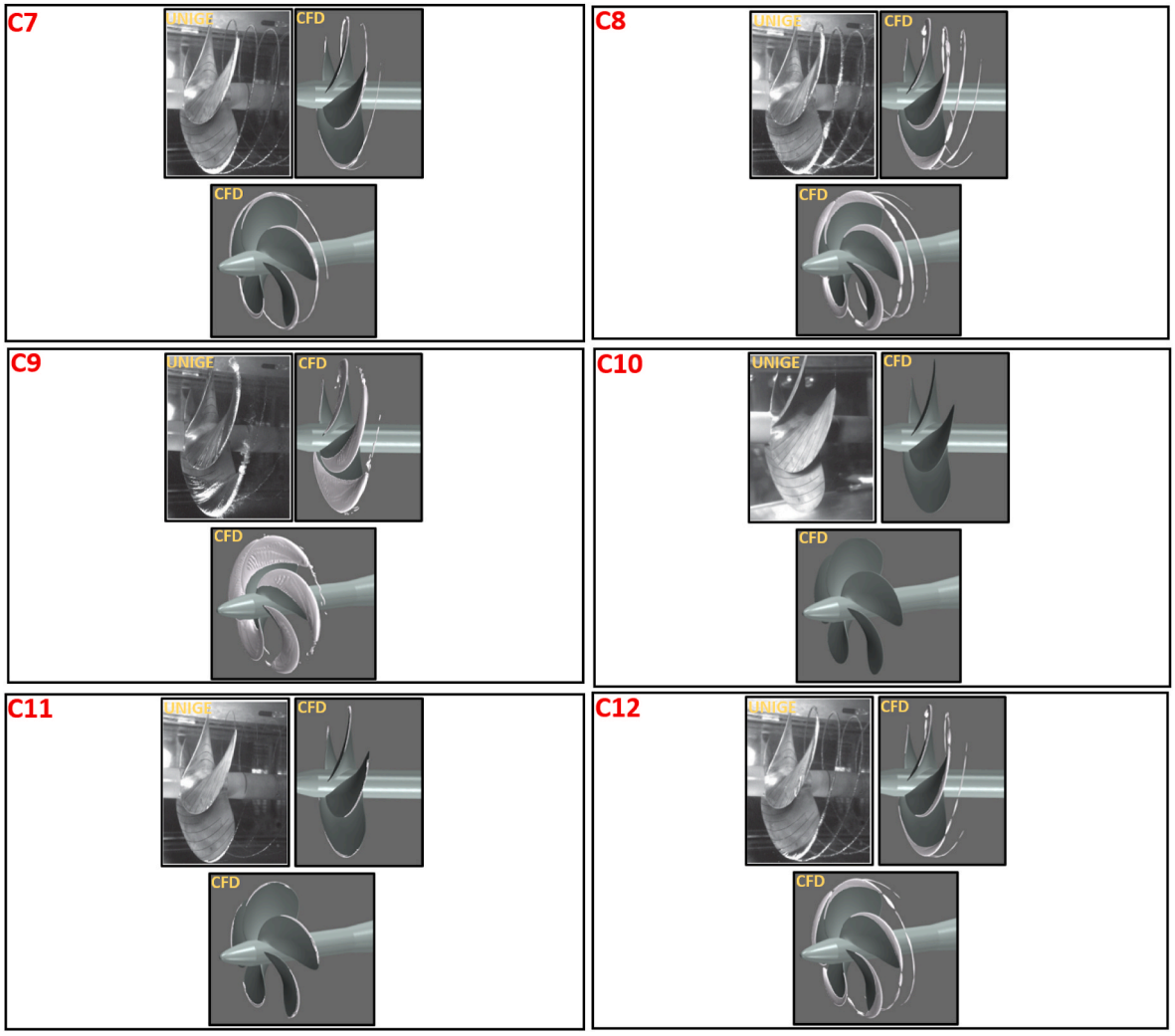

Fig. 8. Comparison of cavitation extensions for inclined shaft configurations (C7, C8, C9, C10, C11 and C12) ($\alpha_v = 0.1$).

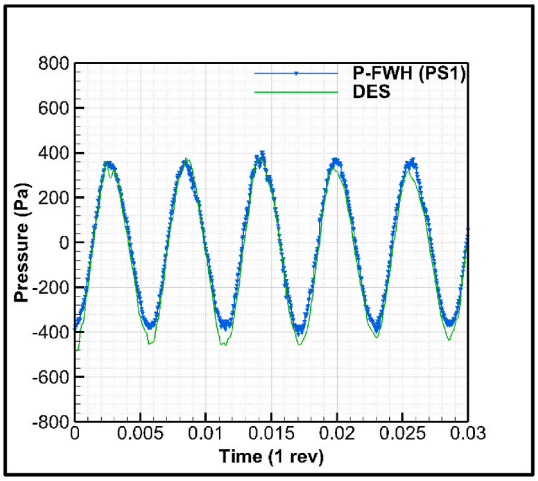

Fig. 9. Comparison of hydrodynamic (DES) and hydroacoustic pressures (P-FWH) in the near field for Condition 2.

4.1.3. Hydroacoustic results

In the hydroacoustic simulations, incompressible hydrodynamic solver (i.e., DES method) and porous FWH formulation were utilised for the propeller URN predictions. The sound speed propagates with the finite speed in a medium under the isentropic flow hypothesis ($c_o^2 = dp/d\rho$). The incompressibility assumption ($d\rho = 0$) denies the acoustic propagation phenomena, and so the simultaneous combination of noise sources overlaps and creates acoustic pressure. This is because the computed pressure at a location is not the resultant value, including all possible pressure waves travelling in the fluid. The acoustic delay affects the contribution of sources in computed pressure and characterises the overall signature of the pressure in terms of amplitude and waveform. This effect is dependent on the relative motion between each source, receiver and sound of speed. As the marine propeller operates at a low rotational speed compared to propagation speed, the acoustic delays become negligible, as shown in the studies of Testa (2008) and Ianniello et al. (2013). Therefore, the instantaneous propagation of sound does not influence the resulting signal considerably in near and mid-field. As a result, despite the theoretical inconsistency of the incompressibility assumption, the comparison of hydrodynamic and hydroacoustic pressures collected close to the noise source can be compared to each other

Table 5
Geometrical properties of selected porous surfaces (L is the length of the PS, D_{PS} is the diameter of the PS).

PS ID	L/D	D_{PS}
1	3.0	1.26D
2	2.5	1.25D
3	2.0	1.24D

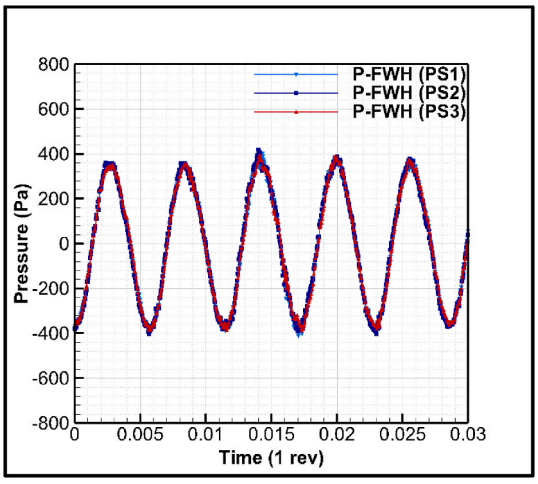

Fig. 10. Comparison of hydroacoustic pressures obtained by different porous surfaces in the near field at the propeller plane (z = 0.17m from the propeller blades' centre) for Condition 2.

to show the reliability of the hydrodynamic and hydroacoustic solution (Testa et al., 2021).

In our study, several receivers are located close to the noise source/porous surface to compare both pressures in the near field for Condition 2. Fig. 9 shows the comparison of the hydrodynamic and hydroacoustic pressures at the propeller plane (i.e., z = 0.17m from the propeller blades' centre). As shown in Fig. 9, the hydrodynamic and hydroacoustic pressures are in good agreement with each other in terms of amplitude and waveform. The agreement between both pressures is present for other receivers located both upstream and downstream of the porous surface.

The placement of porous surfaces is still under debate in the scientific community, and there is no practical guideline for the surface placement and dimensions. Nevertheless, there are few studies recently focused on this subject (e.g., Lidtke et al., 2019b; Testa et al., 2021). The porous surface needs to include all relevant possible numerical noise sources, mainly represented by vorticity and turbulence within the flow domain, especially in the propeller slipstream. For this reason, the permeable surface should be placed in a region where the fine grid resolution is present. The reason behind this is that numerical diffusion in the CFD domain created by the grid resolution can affect the accuracy of the acoustic pressures. In our study, three different permeable surfaces, which have different dimensions and placed in fine grid resolution region, are tested to show the convergence of the solution for Condition 2, as given in Table 5.

The acoustic pressures obtained by different porous/permeable surfaces are first compared in the near field, where the hydrodynamic and hydroacoustic pressures are compared in Fig. 9. As can be seen in Fig. 10, the acoustic pressures are similar in the near field and low-frequency region of the noise spectra.

The acoustic pressures are recorded at the receivers located around the propeller to obtain the noise spectra in narrowband and one-third octave (OTO) band representation. In this study, the propeller URN predictions in the model scale were compared with those of measurements performed by UNIGE. Hence, the receivers are located in the CFD calculations according to the experimental set-up, as shown in Fig. 11.

The measurements were conducted using the receivers H1, H2, and H3. The measurements were presented both averaged of three receivers and only H3. Following this, the data were extrapolated to 1m reference distance using the transfer functions. Akin to the measurements, the CFD calculations were performed using the same three receivers and presented accordingly. The transfer functions were utilised in the measurements to obtain the source strength level (SL), whereas the spherical spreading loss definition (i.e., $20\log(d/d_{ref})$) was adopted in the CFD calculations to extrapolate the results from near (i.e., measured distance, d) to reference distance (i.e., $d_{ref} = 1$m). Additionally, one more receiver was located at 1m in the CFD to compare the results directly without extrapolation from near to far-field. In the experiments, the noise spectra were given in power spectra and the frequency resolution was df = 6.1Hz. Hence, post-processing of the acoustic predictions obtained by CFD was performed similarly for both narrowband and OTO comparison with the measurements.

Before comparing the CFD predictions with the measurements, the convergence of the solution is also investigated at Condition 2 using the permeable surfaces given in Table 5. In this way, the change in the low- and high-frequency part of the spectrum with the application of different permeable surfaces can be seen using the three receivers as in the measurements (see Fig. 11). As shown in Fig. 12, the overall trend of the noise spectra obtained using the three different permeable surfaces is similar for both narrowband and OTO. Yet, slight differences were observed at some BPF values (i.e., 175Hz, 350Hz, 525Hz) predicted by different permeable surfaces. Among them, the PS3 predicted the BPF values slightly more distinct. Thus, it can be concluded that a relatively smaller porous surface (i.e., PS3), which was placed to capture the most energetic part of the vortex and turbulence structures in the propeller slipstream, is likely to capture more noise information than those of

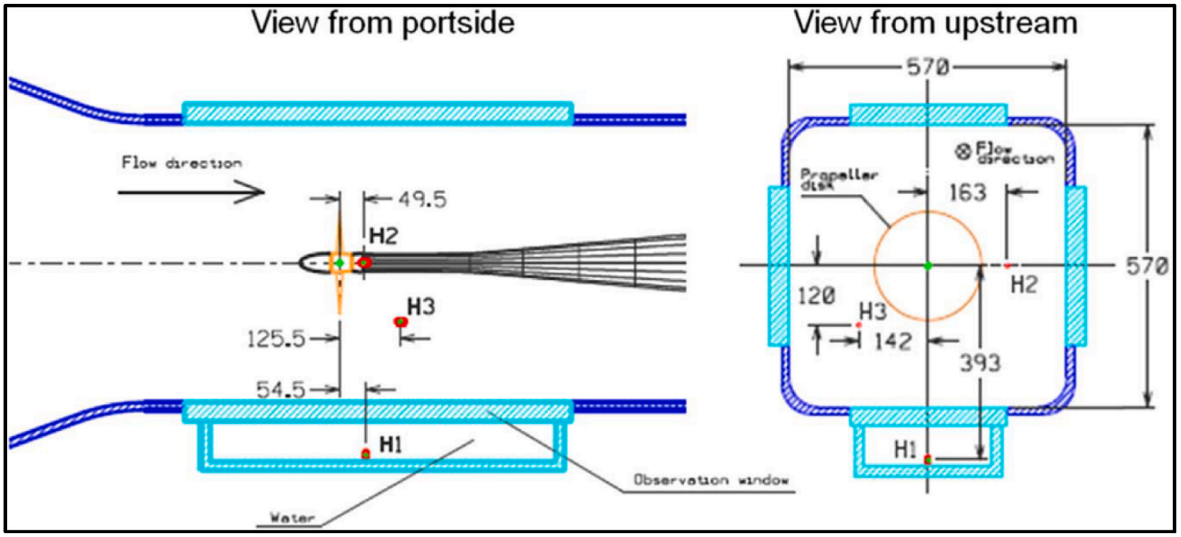

Fig. 11. The receiver locations for the URN measurements during the experiments in UNIGE (Tani et al., 2017).

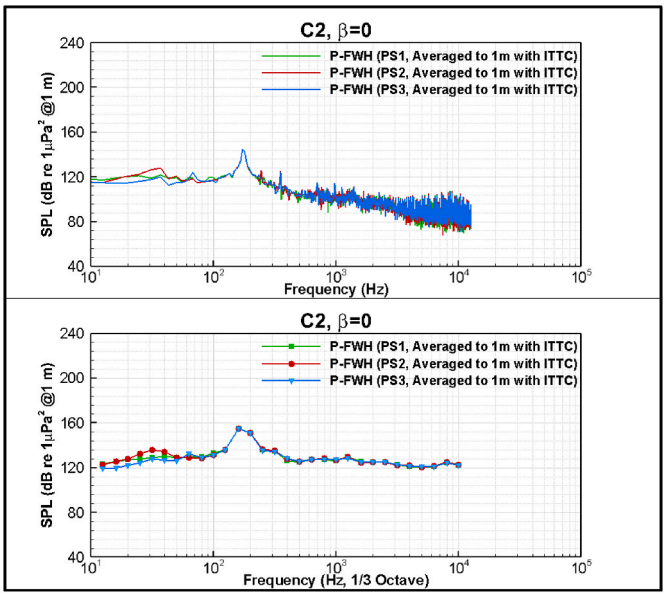

Fig. 12. Comparison of noise spectra obtained by different porous surfaces using the average of three receivers for Condition 2.

relatively bigger porous surfaces. Nevertheless, this needs to be explored with further studies solely focused on this topic. Eventually, the PS3 was used for the comparison of the CFD predictions with the experimental data for the following part of the paper.

Fig. 13 shows the comparison of the predicted noise levels by CFD (i.e., P-FWH) and measurements performed by UNIGE for level flow configurations. The results are presented in both narrowband and OTO for all operating conditions using the average of three receivers and the additional receiver placed at 1m. As shown in Fig. 13, the numerical results underpredict the noise levels between approximately 5 dB and 10 dB for the frequency range between 300Hz and 1 kHz for C1, C2, C4, C5 and C6 compared to measurements. This discrepancy between the numerical prediction and measurements is generally further reduced between 1 kHz and 3 kHz. In some operating conditions, the deviation between CFD and experimental data increased at higher frequencies. This can be associated with the timestep used in the numerical study. The selected timestep might not be sufficient to predict the propeller URN in high frequency region of the noise spectrum. Unlike the C1, C2, C4, C5 and C6, the numerical results are in good agreement with the measurements at C3, particularly until 1 kHz. However, after 1 kHz, the numerical calculations overpredict the noise levels up to approximately 8 kHz. This is likely caused by the large and strong sheet cavitation is observed in the CFD calculations compared to experimental observations obtained in UNIGE. Hence, these cavity dynamics lead to an increase in noise levels between 1 kHz and 8 kHz for C3. In all operating conditions, the 1st BPF (Blade Passage Frequency) values are more distinct at 175Hz in the numerical calculations, whereas the 2nd, 3rd and other peaks are also present but with smaller amplitudes than the peaks from the measured signal. The differences between the average of three receivers and the receiver located at 1m are caused by the extrapolation from near to far-field using the ITTC distance normalisation. Also, the near field effects created by the receiver H2 and H3 can characterise the average of data, especially when the cavitation is not dominant.

In the measurements, the high-amplitude peak was observed around at 740Hz, which was also present in the background noise measurements in the tunnel. According to a detailed investigation conducted by Tani et al. (2017), it was stated that the mechanical vibration of one of the receiver supports created this noise component and it could not be eliminated during the background noise measurements. Also, some other tonal components are distinguishable between 6 kHz and 12 kHz. It was considered that the driveline of the dynamometer probably created these tones, and their amplitude was higher when the propeller was switched to a dummy hub because of the higher loading occurring on the driveline. Thus, these noise components are not relevant for the comparison of numerical calculations with the measurements. A detailed investigation and discussion of the measurements can be found in the study by Tani et al. (2017).

The measured noise data are characterised by a medium-low frequency hump which can be associated with the pressure fluctuations generated by the tip vortex. This spectral hump is partially present at C1, C2, C3, C5 and C6 in the measured data between 300Hz and 1000Hz, although this hump partially overlaps with the irregular peaks due to the tunnel characteristics as stated before. However, the same hump with high amplitude occurs due to the tip vortex pulsation could not be captured in the numerical prediction even though the TVC is modelled in the propeller slipstream using the V-AMR technique. This might be because lack of flow instability in the numerical calculations may not create the cavity volume pulsations using the DES method and Schnerr-Sauer cavitation model under uniform flow conditions compared to experiments. Similar phenomena were also observed under uniform flow conditions, and this resulted in a lack of instability of the cavity and hence propeller URN (Kimmerl et al., 2021).

It is to be noted that the noise predictions for the inclined shaft configurations were not carried out as similar cavitation extents and hydrodynamics characteristics were obtained in the CFD calculations similar to experiments. The comparison of URN results predicted by CFD and measured data for only receiver 3 (i.e., H3) is also given in Appendix A. Similar discrepancies and agreements are found at only receiver 3 between the CFD and experiment.

4.2. Full-scale propeller

In order to compare the numerical results with the measurements performed by different facilities in the scope of the RR test campaign, the URN data needs to be extrapolated from model to full scale, similar to the experiments. The full-scale condition corresponds to the benchmark propeller's operating condition at maximum speed in terms of diameter, shaft rotation and cavitation number. The details of the operating conditions in full-scale are given in Table 6.

where D_S is the diameter, n_S is the propeller rotational rate and σ_{ns} is the cavitation number based on the propeller rotational speed of a full-scale Princess Royal propeller. The prediction of the full-scale propeller URN is made using the procedure given in ITTC, 2017b. In this procedure, the frequency scaling between model and full-scale is given as follows.

$$\frac{f_s}{f_m} = \frac{n_s}{n_m}\cdot\sqrt{\frac{\sigma_s}{\sigma_n}} \tag{10}$$

An increase in Sound Pressure Level (SPL) from model to full-scale is given as:

$$\Delta SPL = 20\log\left[\left(\frac{\sigma_s}{\sigma_n}\right)^w\left(\frac{r_m}{r_s}\right)^x\left(\frac{n_s D_s}{n_m D_m}\right)^y\left(\frac{D_s}{D_m}\right)^z\right] \tag{11}$$

Here, the subscripts s and m refer to full-scale and model scale propellers, respectively. r is the distance between the noise source and receiver. In this procedure, two sets of parameters (w, x, y, z) can be used for the extrapolation and the selection of parameters is dependent on the variation of acoustic efficiency. When the acoustic efficiency is constant, the formulation is known as the high-frequency formulation. Yet, if there is a linear change in acoustic efficiency with the Mach number, the formulation is known as the low-frequency formulation in the extrapolation procedure (ITTC, 2017b).

During the RR test campaign, the low-frequency formulation was used. Hence, the exponents used in the RR test campaign and in this study are given in Table 7 for both constant and proportional bandwidth

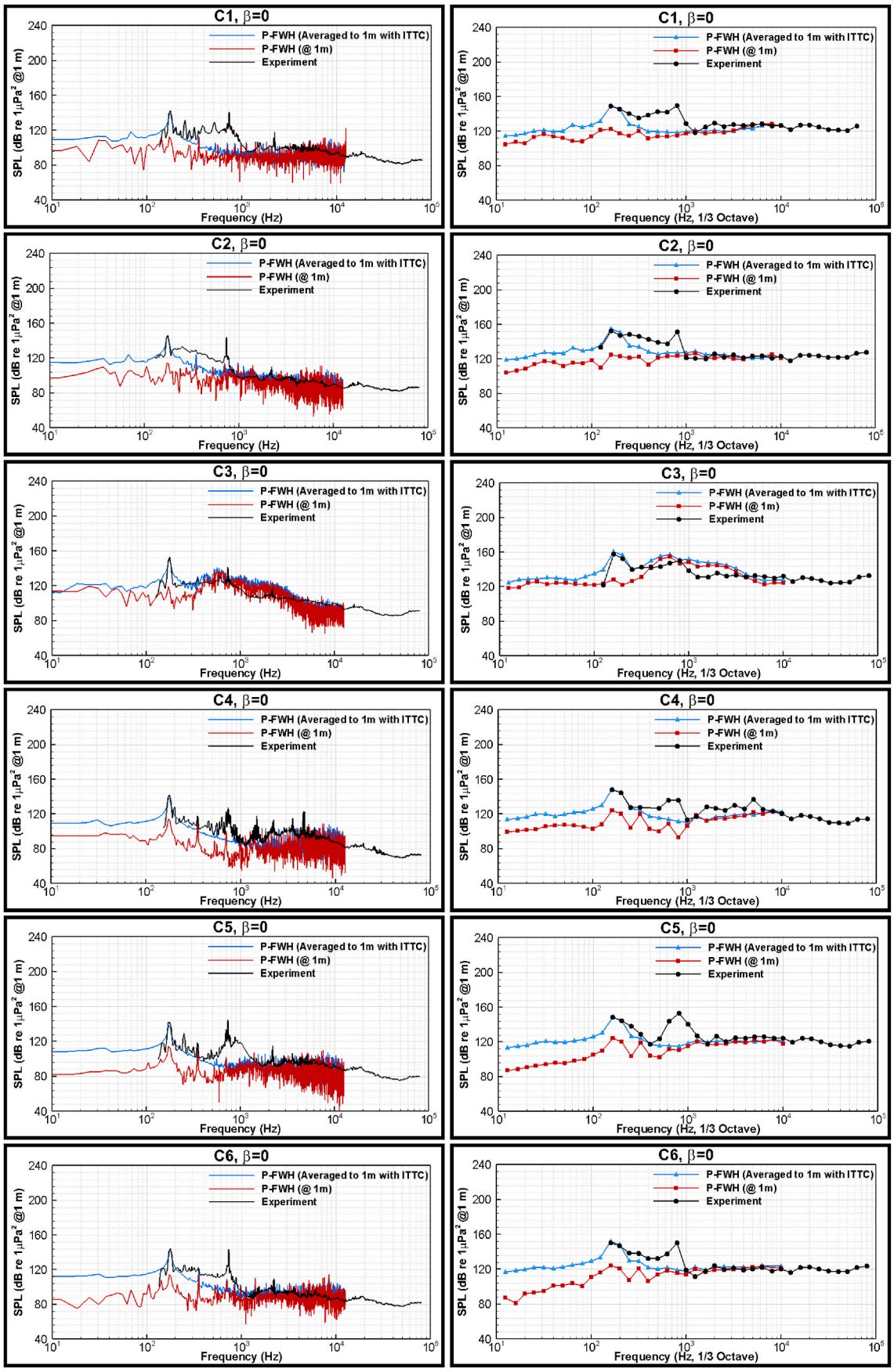

Fig. 13. Comparison of predicted and measured noise levels for level shaft conditions in model scale at all operating conditions.

Table 6
Full-scale propeller operating conditions.

D_S (m)	0.75
n_S (rps)	19.025
σ_s (−)	1.06

Table 7
Exponents for the low-frequency formulation.

Bandwidth	w	x	y	z
Constant	0.75	1	1.5	1.5
Proportional	1	1	2	1

The noise spectra are given in OTO band representation in full-scale and Power Spectral Density (PSD). The full-scale noise spectra are derived using the scaling procedure of ITTC, 2017b, which is briefly explained above, by different facilities and CFD calculations.

spectra.

Before the comparison of numerical predictions with those of measurements by different facilities, the first comparison is carried out using CFD predictions (i.e. P-FWH) for all operating conditions to understand the effects of cavitation dynamics and extensions (see Fig. 5) on propeller URN levels in Fig. 14. The general conclusions can be summarised as follows.

- In general, the increase in cavitation extensions from C1 to C3 and C4 to C5 increases the noise levels accordingly.
- 1st BPF values are generally predicted at all operating conditions with different amplitudes and centred at a slightly different frequency.
- At high blade loading (i.e. $J = 0.4$) conditions, the URN levels show a sudden increase from C1 to C3.
- The largest sheet cavitation observed in C3 manifests itself in higher noise levels among the other conditions.
- At low blade loading conditions (i.e., $J = 0.5$), the highest noise levels are predicted at C6, whereas the lowest noise levels are predicted at C4. The results are in line with the cavitation observations given in Fig. 5.

The comparison of noise predictions obtained by CFD with the measurements carried out by different facilities is given in Fig. 15 for all operating conditions. It should be noted that the measured data were obtained using the data digitiser software. Looking at the comparison of noise data from different facilities reveals that the discrepancies between the noise levels are quite considerable. The distinct tonal components caused by propeller singing, mechanical vibrations, drive train noise etc., were considered to be the main reason for these discrepancies between the measurements in the low-frequency region of the noise spectrum. The contributions of additional noise sources could not be eliminated by the background noise corrections. Similarly, the other noise components (e.g., propeller singing) could not be eliminated as they are part of the overall noise levels Tani et al. (2019). The numerical results generally underpredicted the URN levels compared to measurements by different facilities at C1, C2, C4, C5 and C6, especially until 1 kHz. The predicted noise levels are quite close to the measurements performed by UNIGE, UNEW, MARIN, and CNR for C1, C2 and C6 after 1 kHz. Remarkably, the numerical results slightly overpredict the noise levels at C3 compared to measurements until 1 kHz, whereas the noise levels show a sudden decrease in CFD prediction compared to measurements after 1 kHz. This might be because of the lack of unstructured and cloudy TVC dynamics, which can be the main driven noise sources

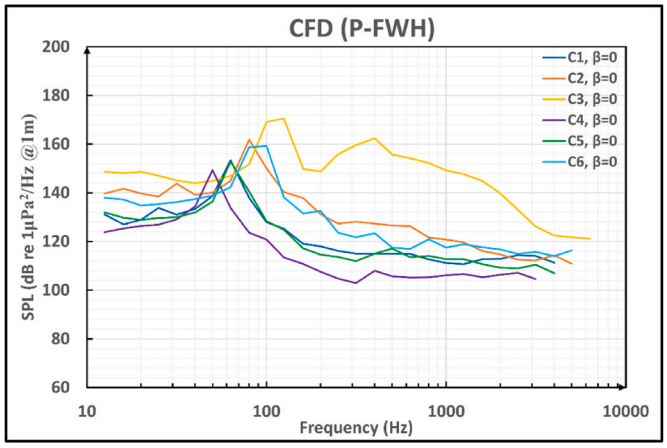

Fig. 14. Comparison of predicted noise levels by CFD for all operating conditions using the average of three receivers.

after 1 kHz, observed in the CFD calculations compared to the measurements.

The interpretation of the CFD results in comparison with the experimental data obtained by different facilities is rather difficult. Even though the cavitation extensions between CFD and experiments are important for the noise predictions, inevitably, there are several possible issues related to the noise propagation process, reverberations and receiver configurations, etc., in the experimental facilities. These differences in the experimental facilities might be the main reason for the noise discrepancies for both each other and CFD. Nevertheless, the CFD results might be evaluated as acceptable in comparison with the measurements by taking the measured margins by all facilities and the uncertainty levels estimated for ship noise predictions based on model tests, which are expected to be 3–5 dB (ITTC, 2017b), into account.

5. Conclusion

In this study, propeller hydrodynamic performance, including cavitation and URN was investigated in a wide range of operating conditions both in model and full-scale using CFD. The selected benchmark propeller was operating under uniform, inclined flow and open water conditions. The cavitating flow around the propeller was solved using the DES method together with the k-ω SST turbulence model, and cavitation on and off the blades was modelled with the Schnerr-Sauer cavitation model. The numerical results were first validated with the experimental data obtained in different facilities through the hydrodynamic performance characteristics and cavitation extensions. Then, propeller URN predictions were performed using the permeable formulation of the FWH equation. The convergence and verification of the URN predictions were shown, and the results were validated on a model scale with the measurements carried out in the UNIGE cavitation tunnel. Then, the propeller URN predictions in model scale were extrapolated to full scale using the ITTC procedure and compared with the measurements conducted at different facilities within the scope of the RR test campaign. Based on the comprehensive verification and validation study, the main findings can be summarised as follows.

- The propeller hydrodynamic performance characteristics (i.e., thrust and torque) were found in good agreement with the experimental data, especially carried out using J identity.
- The sheet cavitation extensions were found similar in CFD compared to the experimental observations, although slight differences were

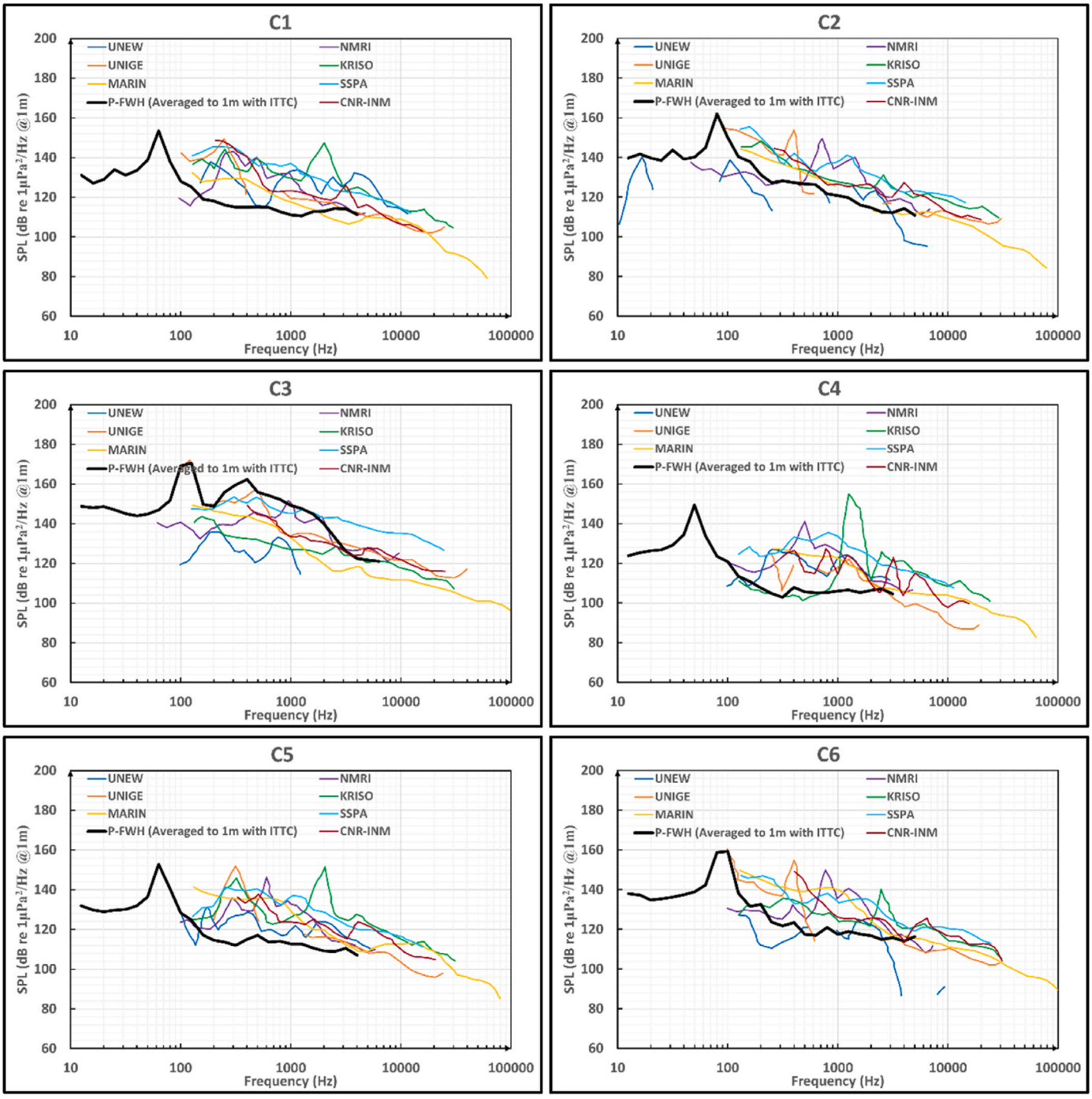

Fig. 15. Comparison of predicted noise and measured noise levels by different facilities (Tani et al., 2019) in the scope of the RR for all operating conditions.

observed in terms of the cavitation extensions towards the inner radii under different operating conditions.

- Tip vortex cavitation (TVC) was successfully modelled in the propeller slipstream using the proposed V-AMR technique in a wide range of operating conditions. However, when the tip vortex diameter was too small according to experimental observation (e.g., C5), the adopted grid size could not capture such a TVC with a small diameter using the V-AMR technique. Thus, the grid size needs to be further reduced for the conditions where the TVC with a small diameter is present.
- The numerical results showed that similar sheet and tip vortex cavitation extensions were observed for the uniform and inclined flow conditions.
- The accuracy of the hydrodynamic and hydroacoustic solution was shown in the verification study. For this purpose, the hydrodynamic and hydroacoustic pressures were compared to each other in a near field (i.e., close to the propeller and permeable noise surface), and good agreement was found between the hydrodynamic and hydroacoustic pressures in the time-domain signal.
- According to a convergence study conducted using different permeable surfaces, it was found that a relatively small permeable noise surface encapsulating the more energetic part of the propeller slipstream captured more noise data.
- The URN predictions in the model scale generally agreed with the measurements with some differences at certain frequency regions. In general, the numerical calculations underpredicted the propeller URN levels around 5 and 10 dB in the low-frequency region compared to measured data. This underprediction of the CFD results can be associated with the lack of spectral hump created by the TVC in the low-frequency region of the noise spectrum. Also, the lack of flow instability and tip vortex dynamics predicted using DES and Schnerr-Sauer cavitation model might be the main reason for this discrepancy between CFD and measured data in the low-frequency region. Therefore, despite the high computational cost, a more advanced model (e.g., LES) together with the advanced cavitation model can be further explored for the propellers operating under uniform flow conditions where the sheet and tip vortex cavitation are present in terms of flow instability and TVC dynamics.
- Although the cavitation tunnel was modelled to replicate the same conditions as in the experiments, the reflections from the tunnel walls could not be taken into account in the CFD calculations. Also, the noise propagation inside the tunnel was not modelled in the numerical calculations. Thus, apart from the differences in cavitation dynamics and hydrodynamic fields between CFD and the experiment, the reflections from the tunnel walls and lack of noise propagation can also be considered other sources for the URN differences between CFD and the experiment.
- The extrapolated propeller URN predictions were also compared with different measured data based on the model scale measurements. The numerical results underpredicted the propeller URN levels compared to measured data by different facilities. Nevertheless, the CFD results can be assessed in acceptable margins by taking the URN level differences measured by different facilities.
- The scaling the URN predictions from model to full-scale using the ITTC procedure will be also investigated to understand the advantages and disadvantageous of the current extrapolation procedure with a study solely focused on this subject.
- The capabilities of the hybrid method (i.e., DES and permeable FWH equation) were shown in terms of propeller URN predictions. Although there were differences in the noise spectrum between the CFD and measurements, the numerical methods can be used for the propeller URN predictions by taking the several differences between experimental conditions and numerical modelling into account.
- On a final note, the URN predictions obtained in this study were achieved using the given numerical methods, including numerical schemes. However, as the cavitation formation and propeller URN predictions might vary with the selection of different numerical schemes and cavitation modelling, it can be useful to investigate the numerical parameters used in the numerical calculations in detail. Also, within the availability of the computational resources, the compressible flow solver can be adapted to predict the propeller URN.

CRediT authorship contribution statement

Savas Sezen: Conceptualization, Methodology, Software, Validation, Investigation, Resources, Data curation, Writing – original draft, preparation, Writing – review & editing, Visualization. **Mehmet Atlar:** Investigation, Resources, Writing – review & editing, Supervision, Project administration.

Declaration of competing interest

The authors declare that they have no known competing financial interests or personal relationships that could have appeared to influence the work reported in this paper.

Data availability

No data was used for the research described in the article.

Acknowledgements

The first author was sponsored by Stone Marine Propulsion Ltd of the UK and the University of Strathclyde during his PhD study. Results were obtained using the ARCHIE-WeSt High-Performance Computer (www.archie-west.ac.uk) based at the University of Strathclyde. The authors also thank Dr Giorgio Tani for providing the experimental data and participants in the ongoing RR test campaign.

Appendix A

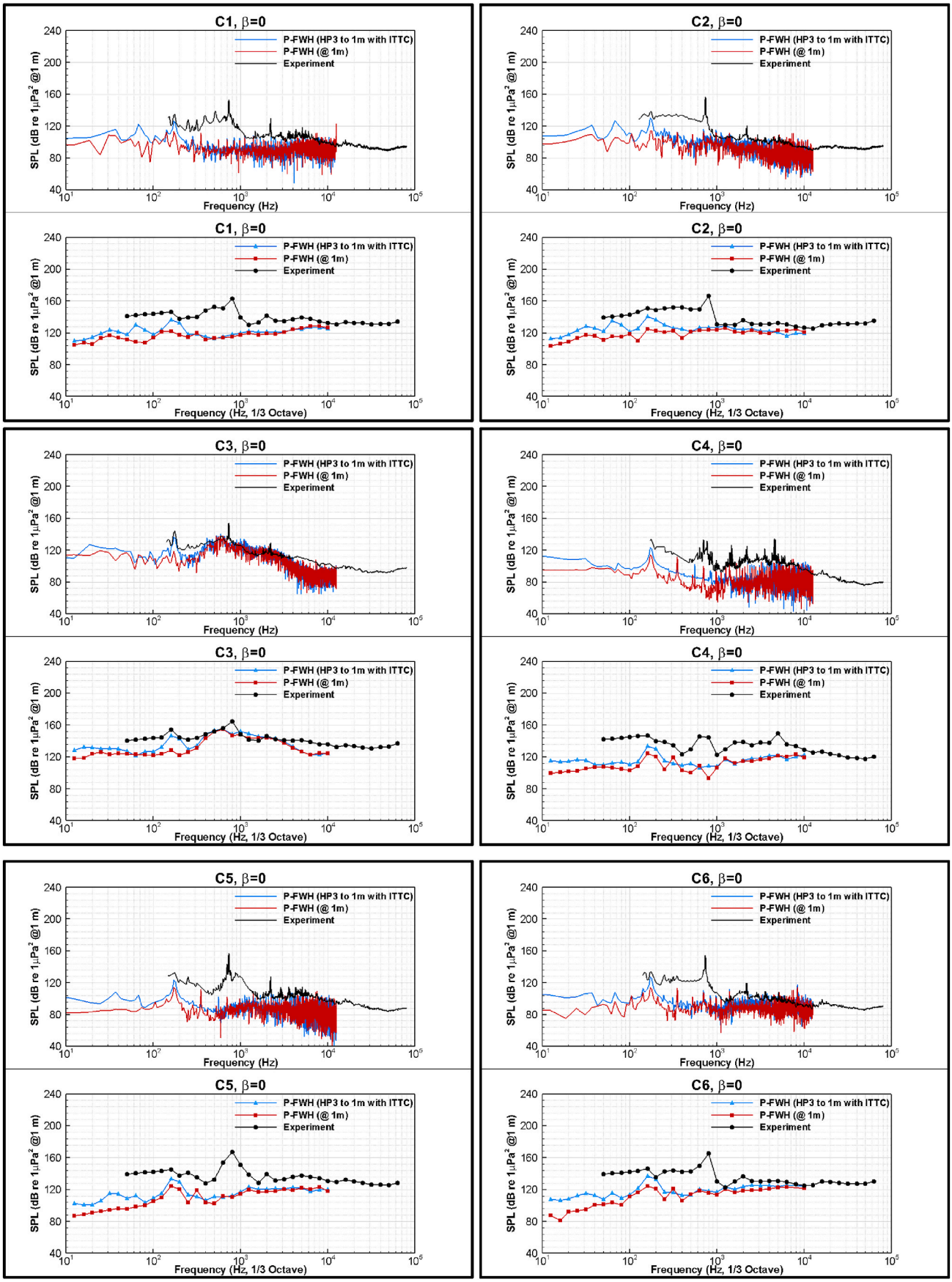
C1, β=0
C2, β=0
C3, β=0
C4, β=0
C5, β=0
C6, β=0
P-FWH (HP3 to 1m with ITTC)
P-FWH (@ 1m)
Experiment
SPL (dB re 1μPa² @1 m)
Frequency (Hz)
Frequency (Hz, 1/3 Octave)

References

Abrahamsen, K., 2012. The ship as an underwater noise source. In: Proceedings of Meetings on Acoustics. https://doi.org/10.1121/1.4772953. Edinburgh, UK.

Aktas, B., Atlar, M., Turkmen, S., Korkut, E., Fitzsimmons, P., 2016. Systematic cavitation tunnel tests of a Propeller in uniform and inclined flow conditions as part of a round robin test campaign. Ocean Eng. 120, 136–151. https://doi.org/10.1016/j.oceaneng.2015.12.015.

AMT'11, 2011. In: 2nd International Conference on Advanced Model Measurement Technology for the EU Maritime Industry. Newcastle University, Newcastle Upon Tyne. AMT'11.

AQUO, 2012. Achieve Quiter Oceans by shipping noise footprint reduction. In: 7th Framework Program. Grant agreement ID, 314227.

Atlar, M., Aktas, B., Samspon, R., Fitzsimmons, P., Fetherstonhaug, C., 2013. A multi-purpose marine science and technology research vessel for full-scale observations and measurements. In: 3rd International Conference on Advanced Model Measurement Technologies for the Marine Industry. AMT`13, Gdansk, Poland.

Bosschers, J., 2018. Propeller Tip-Vortex Cavitation and its Broadband Noise, PhD Thesis. Universtiy of Twente.

Brentner, K.S., Farassat, F., 2003. Modeling aerodynamically generated sound of helicopter rotors. Prog. Aero. Sci. 39, 83–120. https://doi.org/10.1016/S0376-0421(02)00068-4.

Chou, E., Southall, B.L., Robards, M., Rosenbaum, H.C., 2021. International policy, recommendations, actions and mitigation efforts of anthropogenic underwater noise. Ocean Coast Manag. 202, 105427 https://doi.org/10.1016/J.OCECOAMAN.2020.105427.

Curle, N., 1955. The influence of solid boundaries upon aerodynamic sound. Proc. R. Soc. London. Ser. A. Math. Phys. Sci. 231, 505–514. https://doi.org/10.1098/rspa.1955.0191.

Di Francescantonio, P., 1997. A new boundary integral formulation for the prediction of sound radiation. J. Sound Vib. 202, 491–509. https://doi.org/10.1006/jsvi.1996.0843.

DNV, 2010. Rules for Classification of Ships, New Buildings. Part 6 (Chapter 24).

Farassat, F., 2007. Derivation of formulations 1 and 1A of Farassat. NASA/TM-2007-214853 1–25.

Ffowcs Williams, J., 1992. Noise source mechanisms. In: Modern Methods in Analytical Acoustics. Lecture Notes. Springer, Berlin, pp. 313–354.

Ffowcs Williams, J.H., Hawkings, D.L., 1969. Sound generation by turbulence and surfaces in arbitrary motion. Philos. Trans. R. Soc. London. Ser. A, Math. Phys. Sci. 264, 321–342. https://doi.org/10.1098/rsta.1969.0031.

Heise, K., Alidina, H., 2012. Summary Report: Ocean Noise in Canada's Pacific Workshop. Canada, Vancouver. January 31, February 1.

Hildebrand, J., 2005. Impacts of anthropogenic sound. In: Marine Mammal Research: Conservation beyond Crisis. The Johns Hopkins University Press, Baltimore, Maryland, pp. 101–124.

Hildebrand, J., 2004. Sources of anthropogenic sound in the marine environment. In: International Policy Workshop on Sound and Marine Mammals, 28–30 September (London, UK).

Ianniello, S., De Bernardis, E., 2015. Farassat's formulations in marine propeller hydroacoustics. Int. J. Aeroacoustics 14, 87–103.

Ianniello, S., Muscari, R., Di Mascio, A., 2013. Ship underwater noise assessment by the acoustic analogy. Part I: nonlinear analysis of a marine propeller in a uniform flow. J. Mar. Sci. Technol. 18, 547–570. https://doi.org/10.1007/s00773-013-0227-0.

Ikeda, T., Enomoto, S., Yamamoto, K., Amemiya, K., 2017. Quadrupole corrections for the permeable-surface Ffowcs williams–Hawkings equation. AIAA 55, 2307–2320. https://doi.org/10.2514/1.J055328.

IMO, 2014. MEPC.1/Circ.833: Guidelines for the Reduction of Underwater Noise from Commercial Shipping to Address Adverse Impacts on Marine Life.

ITTC, 2017a. Specialist Committee on Hydrodynamic Noise Final Report and Recommendations to the 28th ITTC (Copenhagen, Denmark).

ITTC, 2017b. Model-Scale Propeller Cavitation Noise Measurements, vol. 7, p. 5, 02-01-05.

Kimmerl, J., Mertes, P., Abdel-Maksoud, M., 2021. Application of large eddy simulation to predict underwater noise of marine propulsors. Part 2: noise generation. J. Mar. Sci. Eng. 778. https://doi.org/10.3390/JMSE9070778, 2021, Vol. 9, Page 778 9.

Lidtke, A.K., Lloyd, T., Vaz, G., 2019a. Acoustic modelling of a propeller subject to non-uniform inflow. In: Sixth International Symposium on Marine Propulsors, SMP'2019 (Rome, Italy).

Lidtke, Artur K., Vaz, G., Lloyd, T., 2019b. Acoustic Modelling of a Propeller Subject to Non-uniform Inflow. In: Sixth International Symposium on Marine Propulsors, vol. 19. Italy, Rome smp.

Lidtke, A.K., Turnock, S.R., Humphrey, V.F., 2015. Use of acoustic analogy for marine propeller noise characterisation. In: Fourth International Symposium on Marine Propulsors SMP'15. Austin, Texas, USA.

Lighthill, M.J., 1952. On sound generated aerodynamically I. General theory. Proc. R. Soc. London. Ser. A. Math. Phys. Sci. 211, 564–587. https://doi.org/10.1098/rspa.1952.0060.

Lloyd, T.P., Rijpkema, D., Van Wijngaarden, E., 2014. Implementing the Ffowcs Williams-Hawkings acoustic analogy into a viscous CFD solver PROCAL. In: Numerical Towing Tank Symposium. NuTTS'2014. Gotherburg, Sweden.

Nitzkorski, Z., 2015. A Novel Porous Ffowcs-Williams and Hawkings Acoustic Methodology for Complex Geometries, PhD Thesis. Faculty of the Graduate School of the University of Minnesota.

SATURN, 2021. Solutions @ Underwater Radiated Noise Grant Agreement ID, 101006443.

Schnerr, G.H., Sauer, J., 2001. Physical and numerical modeling of unsteady cavitation dynamics. In: 4th International Conference on Multiphase Flow. New Orleans, USA.

Seol, H., Suh, J.C., Lee, S., 2005. Development of hybrid method for the prediction of underwater propeller noise. J. Sound Vib. 288, 345–360. https://doi.org/10.1016/j.jsv.2005.01.015.

Sezen, S., Atlar, M., 2021. An alternative Vorticity based Adaptive Mesh Refinement (V-AMR) technique for tip vortex cavitation modelling of propellers using CFD methods. Ship Technol. Res. 69, 1–21. https://doi.org/10.1080/09377255.2021.1927590.

Sezen, S., Atlar, M., Fitzsimmons, P., 2021a. Prediction of cavitating propeller underwater radiated noise using RANS & DES-based hybrid method. Ships Offshore Struct. 16, 93–105. https://doi.org/10.1080/17445302.2021.1907071.

Sezen, S., Cosgun, T., Yurtseven, A., Atlar, M., 2021b. Numerical investigation of marine propeller Underwater Radiated Noise using acoustic analogy part 1: the influence of grid resolution. Ocean Eng. 220, 108448 https://doi.org/10.1016/j.oceaneng.2020.108448.

Sezen, S., Cosgun, T., Yurtseven, A., Atlar, M., 2020. Numerical investigation of marine propeller underwater radiated noise using acoustic analogy part 2: the influence of eddy viscosity turbulence models. Ocean Eng. 220, 108353 https://doi.org/10.1016/j.oceaneng.2020.108353.

SONIC, 2012. Suppression of underwater noise induced by cavitation. EC-FP7, Grant Agreement No, 2012 314394.

Spalart, P.R., Jou, W.-H., Strelets, M., Allmaras, S.R., 1997. Comments on the feasibility of LES for wings, and on a hybrid RANS/LES approach. Research, U.S.A.F.O. of S.. In: Proceedings of First AFOSR International Conference on DNS/LES. Greyden Press, Siemens. Star CCM+ 14.06, 2019. User Guide.

Stark, C., Shi, W., 2021. Hydroacoustic and hydrodynamic investigation of bio-inspired leading-edge tubercles on marine-ducted thrusters. R. Soc. Open Sci. 8, 210402 https://doi.org/10.1098/RSOS.210402.

Tani, G., Aktas, B., Viviani, M., Atlar, M., 2017. Two medium size cavitation tunnel hydro-acoustic benchmark experiment comparisons as part of a round robin test campaign. Ocean Eng. 138, 179–207. https://doi.org/10.1016/j.oceaneng.2017.04.010.

Tani, G., Viviani, M., Felli, M., Lafeber, F.H., Lloyd, T., Aktas, B., Atlar, M., Turkmen, S., Seol, H., Hallander, J., Sakamoto, N., 2020. Noise measurements of a cavitating propeller in different facilities: results of the round robin test programme. Ocean Eng. 213, 107599 https://doi.org/10.1016/j.oceaneng.2020.107599.

Tani, G., Viviani, M., Felli, M., Lafeber, F.H., Lloyd, T., Atlar, M., Seol, H., Hallander, J., Sakamoto, N., Kamiirisa, H., 2019. Round robin test on radiated noise of a cavitating propeller. In: Proceedings of 6th International Symposium on Marine Propulsors, SPM'19 (Rome, Italy).

Testa, C., 2008. Acoustic Formulations for Aeronautical and Naval Rotorcraft Noise Prediction Based on the Ffowcs Williams and Hawkings Equation. Delft University of Technology, TUD.

Testa, C., Porcacchia, F., Zaghi, S., Gennaretti, M., 2021. Study of a FWH-based permeable-surface formulation for propeller hydroacoustics. Ocean Eng. 240, 109828 https://doi.org/10.1016/J.OCEANENG.2021.109828.

Testa, C., Procacchia, F., Greco, L., Muscari, R., 2018. Effectiveness of boundary element method hydrodynamic data for propeller hydroacoustics. In: A. Yucel Odabasi Colloquium Series 3rd International Meeting-Progress in Propeller Cavitation and its Consequences. Istanbul, Turkey.

Wang, M., Lele, S.K., Moin, P., 1996. Computation of quadrupole noise using acoustic analogy. AIAA J. 34, 2247–2254. https://doi.org/10.2514/3.13387.